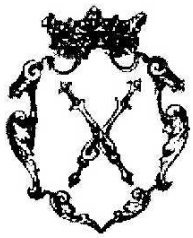
JAGIELLONIAN UNIVERSITY
INSTITUTE OF PHYSICS



Search for the $\mathcal{CP}$ symmetry violation in the decays of K_S mesons using the KLOE detector

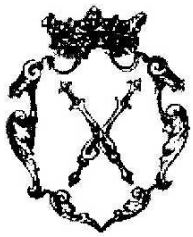
Michał Silarski

PhD thesis prepared in the Department of Nuclear Physics
of the Jagiellonian University under supervision
of Prof. Paweł Moskal

Cracow 2012

arXiv:1302.4427v1 [hep-ex] 19 Feb 2013

UNIWERSYTET JAGIELLOŃSKI
INSTYTUT FIZYKI



Poszukiwania łamania symetrii CP w rozpadach mezonu K_S za pomocą detektora KLOE

Michał Silarski

Praca doktorska wykonana w Zakładzie Fizyki Jądrowej
Uniwersytetu Jagiellońskiego pod kierunkiem
Prof. dr hab. Pawła Moskala

Kraków 2012

„ Nur ein Leben für die anderen ist lebenswert ”

Albert Einstein

Abstract

The aim of this work was to determine the $K_S \to 3\pi^0$ decay branching ratio and a modulus of the η_{000} parameter, defined as the ratio of amplitudes for $K_S \to 3\pi^0$ to $K_L \to 3\pi^0$ decays, which characterizes the $\mathcal{CP}$ symmetry violation in this decay.
The measurement has been carried out with the KLOE detector operating at the ϕ – factory DAΦNE in the Italian National Center for Nuclear Physics in Frascati. DAΦNE collides the e^+ and e^- beams at the center of mass energy $\sqrt{s} = 1019.45$ MeV. The e^+e^- collisions result in the ϕ meson creation which is almost at rest and decay predominantly to kaon pairs. The decay products are registered using the KLOE detection setup, which consists of large cylindrical drift chamber surrounded by the electromagnetic calorimeter. The detectors are placed in a magnetic field of $B \approx 0.52$ T generated by superconducting solenoid. The K_S mesons were identified with high efficiency via registration of these K_L mesons which crossed the drift chamber without decaying and then interacted with the KLOE electromagnetic calorimeter. The K_S four – momentum vector was then determined using the registered position of the K_L meson and the known momentum of the ϕ meson. Next, the search for the $K_S \to 3\pi^0 \to 6\gamma$ decay was carried out by the selection of events with six gamma quanta which momenta were reconstructed using time and energy measured by the electromagnetic calorimeter. To increase the signal over background ratio after identification of the K_S meson and requiring six reconstructed photons a discriminant analysis is performed. It is based on kinematical fit, testing of the signal and background hypotheses and exploiting of the differences in kinematics of the K_S decays into $2\pi^0$ and $3\pi^0$.
The search for the $K_S \to 3\pi^0$ decay presented in this work failed to detect a signal of sufficient statistical significance. Hence, we have obtained the upper limit on the $K_S \to 3\pi^0$ branching ratio at the 90% confidence level:

$$BR(K_S \to 3\pi^0) \leq 2.7 \cdot 10^{-8} \, ,$$

which is almost five times lower than the latest published result. This upper limit can be translated into a limit on the modulus of the η_{000} parameter amounting to: $|\eta_{000}| \leq 0.009$ at the 90% confidence level. This corresponds to an improvement of the $|\eta_{000}|$ uncertainty by a factor of two with respect to the latest direct measurement.
The upper limit on the $K_S \to 3\pi^0$ branching ratio determined in this work is still about one order of magnitude larger than the prediction based on the Standard Model. Hence, the search for this decay will be continued with the upgraded KLOE detector, which has realistic chances to observe the $K_S \to 3\pi^0$ decay for the first time in the near future.

Streszczenie

Celem tej pracy było wyznaczenie stosunku rozgałęzień dla rozpadu $K_S \to 3\pi^0$, oraz modułu parametru η_{000}, zdefiniowanego jako stosunek amplitud na rozpad $K_S \to 3\pi^0$ i $K_L \to 3\pi^0$, który charakteryzuje niezachowanie symetrii $\mathcal{CP}$ w tym procesie.
Pomiary wspomnianego rozpadu były prowadzone za pomocą detektora KLOE działającego na akceleratorze wiązek przeciwbieżnych DAΦNE we Włoskim Narodowym Centrum Fizyki Jądrowej we Frascati. DAΦNE zderza wiązki e^+ e^- przy energii w centrum masy $\sqrt{s} = 1019.45$ MeV równej masie mezonu ϕ. W wyniku zderzeń e^+e^- powstają mezony ϕ. Produkowane są one praktycznie w spoczynku i rozpadają się głównie na pary kaonów. Do pomiaru powstających cząstek wykorzystywany jest układ detekcyjny KLOE. Zbudowany jest on z cylindrycznej komory dryfowej otoczonej kalorymetrem elektromagnetycznym. Całość umieszczona jest w polu magnetycznym nadprzewodzącego solenoidu o indukcji $B \approx 0.52$ T. Mezony K_S identyfikowane były z dużą wydajnością poprzez rejestrację tych mezonów K_L, które nie rozpadły się w komorze dryfowej i zareagowały z materiałem kalorymetru elektromagnetycznego. Wektor czteropędu mezonu K_S określany był na podstawie zarejestrowanej w kalorymetrze pozycji mezonu K_L i znanego wektora czteropędu mezonu ϕ. Poszukiwania rozpadów $K_S \to 3\pi^0 \to 6\gamma$ prowadzone były następnie poprzez wybranie zdarzeń z sześcioma zrekonstruowanymi kwantami gamma. Ich pędy określane były na podstawie czasu i energii mierzonych za pomocą kalorymetru. Aby zwiększyć stosunek sygnału do tła zdarzenia ze zidentyfikowanym mezonem K_S i sześcioma zrekonstruowanymi kwantami gamma zostały poddane dalszej analizie, opartej na dopasowaniu kinematycznym, testowaniu hipotez tła i sygnału oraz wykorzystaniu różnic w kinematyce rozpadów mezonu K_S na dwa i trzy mezony π^0.
W wyniku przeprowadzonych poszukiwań nie zarejestrowano żadnego zdarzenia odpowiadającego rozpadowi $K_S \to 3\pi^0$. Dlatego określono górną granicę stosunku rozgałęzień dla rozpadu $K_S \to 3\pi^0$ na poziomie ufności 90%:

$$BR(K_S \to 3\pi^0) \leq 2.7 \cdot 10^{-8} \, .$$

Otrzymana wartość jest około pięć razy niższa od ostatniej opublikowanej górnej granicy na ten stosunek rozgałęzień. Otrzymana na poziomie ufności 90% wartość górnej granicy dla modułu parametru η_{000} wynosi: $|\eta_{000}| \leq 0.009$, co odpowiada zmniejszeniu jego niepewności dwa razy w stosunku do ostatniego bezpośredniego pomiaru.
Otrzymana wartość górnej granicy na $BR(K_S \to 3\pi^0)$ jest większa od teoretycznych przewidywań o rząd wielkości, dlatego poszukiwania tego rozpadu będą kontynuowane za pomocą systemu detekcyjnego KLOE wyposażonego w nowe detektory.

Contents

1 Introduction **1**

2 Neutral Kaon system and $\mathcal{CP}$ violation **5**
2.1 The neutral kaon system 6
2.2 $\mathcal{CP}$ violation in kaon decays 8

3 The KLOE experiment at DAΦNE **13**
3.1 The DAΦNE Collider 13
3.2 The KLOE detector 14
3.2.1 The Drift Chamber 15
3.2.2 The Electromagnetic Calorimeter 17
3.2.3 The Trigger system 20

4 First stage of the event selection **23**
4.1 Identification of K_S via detection of K_L 23
4.1.1 Identification of the K_L meson 24
4.1.2 K_L – momentum estimate 26

5 Normalization sample **27**
5.1 Comparison between data and simulations results for 4γ events 29
5.2 Background estimation and counting of the $K_S \to 2\pi^0 \to 4\gamma$ events . 35

6 Search for the $K_S \to 3\pi^0 \to 6\gamma$ signal **37**
6.1 Discriminating variables and the signal region definition 38
6.1.1 Rejection of the $K_L \to 3\pi^0$ events 38
6.1.2 The kinematical fit 39
6.1.3 Testing the $3\pi^0$ and $2\pi^0$ hypotheses 41
6.1.4 Improvement of the $K_S \to 2\pi^0$ background suppression . . . 43
6.2 Background estimation 45
6.2.1 Event weights determination 45
6.3 Optimization of selection criteria 49

6.4 Counting of the $K_S \to 3\pi^0$ events 51

7 Systematic error estimation **55**
7.1 Systematics related to acceptance for the $K_S \to 2\pi^0$ channel 55
7.2 Systematics related to the selection efficiency and background for the $K_S \to 3\pi^0$ channel 58
7.3 Correction for the different K_S tagging efficiencies for the $K_S \to 3\pi^0$ and $K_S \to 2\pi^0$ decays 62

8 Upper limit on the $K_S \to 3\pi^0$ branching ratio and $|\eta_{000}|$ **63**
8.1 Upper limit on the measured number of $K_S \to 3\pi^0$ decays 63
8.2 Determination of the upper limits on the $K_S \to 3\pi^0$ branching ratio and $|\eta_{000}|$ 65

9 Summary and outlook **67**

Acknowledgments **71**

Bibliography **73**

Chapter 1

Introduction

In 1918 Amalie Emmy Noether proved a theorem connecting the symmetries of the physical systems and conservation laws [1] which became one of the greatest achievements of the twentieth century theoretical physics. It shows for instance that a system invariant under translations of time, space, or rotation will obey the laws of conservation of energy, linear momentum, or angular momentum, respectively. From that time on the symmetries have become an essential part of almost all physics theories and models, especially in the particle physics. And so for example every quantum field theory describing the interaction and properties of elementary particles are formulated requiring the Lorentz invariance. Furthermore, the discrete symmetries of Parity $\mathcal{P}$, Charge Conjugation $\mathcal{C}$ and Time Reversal $\mathcal{T}$ proved to be very useful in the calculation of the cross sections and decay rates, especially for the processes governed by the strong interaction. These symmetries became also an important tool in the Standard Model formulation.

Among the known elementary forces the weak interaction has appeared to be very peculiar mainly because it violates $\mathcal{P}$ and $\mathcal{C}$ symmetries [2, 3] as well as their combination: $\mathcal{CP}$. The $\mathcal{CP}$ violation was discovered unexpectedly in 1964 by Christenson, Cronin, Fitch and Turlay during the regeneration studies of the neutral K mesons [4]. In the framework of Standard Model the $\mathcal{CP}$ violation mechanism is introduced by the quark mixing described by the complex Cabibbo – Kobayashi – Maskawa matrix with one nonzero phase [5, 6], which requires the existence of three generation of quarks. Parameters describing the $\mathcal{CP}$ violation in the neutral kaon system were measured with a good precision by several experiments [7–9], and at present the main experimental effort is focused on studies of the neutral B and D meson systems [10–13]. However, there are still several interesting open issues in the kaon physics. One of them is the $K_S \to 3\pi^0$ decay which, assuming the $\mathcal{CPT}$ invariance, allows one to investigate the direct $\mathcal{CP}$ symmetry violation [14]. Despite several direct searches [15, 16] and $K_S K_L$

interference studies [17, 18], this decay remains undiscovered and the best upper limit on the branching ratio $BR(K_S \to 3\pi^0) < 1.2 \cdot 10^{-7}$ [16, 19] is still two orders of magnitude larger than the predictions based on the Standard Model [14].

This work is focused on the measurement of the $K_S \to 3\pi^0$ decay branching ratio based on the data sample gathered in 2004 – 2005 with the KLOE detector operating at the ϕ – factory DAΦNE in the Italian National Center for Nuclear Physics in Frascati. DAΦNE collides the e^+ and e^- beams at the center of mass energy of $\sqrt{s}$ = 1019.45 MeV near the ϕ meson mass [20]. The e^+e^- collisions result in ϕ meson creation which is almost at rest ($\beta_\phi \approx 0.015$) and decay predominantly to K^+K^- (49%), K_SK_L (34%), $\rho\pi$ (15%) and $\eta\gamma$ (1.3%) final states [19]. The decay products are registered using the KLOE detection setup, which consists of large cylindrical drift chamber surrounded by the electromagnetic calorimeter. The detectors are placed in a magnetic field of $B \approx 0.52$ T generated by superconducting solenoid. Since the ϕ mesons are produced almost at rest, kaons arising from the decay move with the relative angle close to 180^0, and as a consequence, their decay products are registered in the well separated parts of the detector. The K_S mesons are identified with high efficiency ($\sim$ 34%) via registration of these K_L mesons which cross the drift chamber without decaying and then interact with the KLOE electromagnetic calorimeter (so called K_S tag). The K_S four – momentum vector is then determined using the registered position of the K_L meson and the known momentum of the ϕ meson, which is estimated as an average of the momentum distribution measured using large angle e^+e^- scattering. The search for the $K_S \to 3\pi^0 \to 6\gamma$ decay is then carried out by the selection of events with six γ quanta which momenta are reconstructed using time and energy measured by the electromagnetic calorimeter. Background for the searched decay originates mainly from the $K_S \to 2\pi^0$ events with two spurious clusters from fragmentation of the electromagnetic showers (so called splitting) or accidental activity, or from false K_L identification [21]. To increase the signal over background ratio after identification of the K_S meson and requiring six reconstructed photons a discriminant analysis is performed. It is based on kinematical fit, testing of the signal and background hypotheses and exploiting of the differences in kinematics of the K_S decays into $2\pi^0$ and $3\pi^0$.

This thesis is divided into nine chapters. The detailed description of the $\mathcal{CP}$ violation mechanism in the neutral kaon system is presented in the second chapter together with the motivation to search for the $K_S \to 3\pi^0$ decay.
The third chapter provides the description of experimental tools used for the measurement: the DAΦNE collider, the KLOE detector as well as the trigger and data acquisition system.

The method used to identify the K_S mesons based on the detection of the K_L interactions in the electromagnetic calorimeter is presented in chapter four.
Chapter five is devoted to the identification of the $K_S \to 2\pi^0$ events used for the normalization of the measured branching ratio.
The discriminant analysis used to increase the signal over background ratio is described in chapter six, where also the background estimation based on the Monte Carlo simulations and the final result of the $K_S \to 3\pi^0$ identification are presented.
The seventh chapter is devoted to the estimation of the systematic uncertainties of the measurement.
The determined upper limit on the $K_S \to 3\pi^0$ branching ratio is given in chapter eight together with the estimation of the modulus of the η_{000} parameter, defined as the ratio of amplitudes for $K_S \to 3\pi^0$ to $K_L \to 3\pi^0$ decays.
Finally, the ninth chapter comprises the summary and perspectives. In particular we discuss the possibility of the first observation of the $K_S \to 3\pi^0$ decay in the next KLOE–2 data – taking campaign during 2013 – 15. It will be conducted with the KLOE detector upgraded by Inner Tracker and with improved photon acceptance brought about by new calorimeters installed in the final focusing region.

Chapter 2

Neutral Kaon system and $\mathcal{CP}$ violation

Discrete symmetries as parity $\mathcal{P}$, charge conjugation $\mathcal{C}$ and time reversal $\mathcal{T}$, as well as their combinations such as $\mathcal{CP}$ and $\mathcal{CPT}$ play a fundamental role in particle physics. The parity transformation $\mathcal{P}$ changes the signs of the three space coordinates, while $\mathcal{C}$ changes particle to its antiparticle and vice versa changing its internal quantum numbers. The strong and electromagnetic interaction preserve eigenvalues of both, parity and charge conjugation operators, as well as eigenvalues of the $\mathcal{CP}$ operator. The weak interaction instead do not preserve these quantum numbers which result in a far – reaching consequences, especially in case of the $\mathcal{CP}$ operator. In the framework of the Standard Model the $\mathcal{CP}$ violation implies the existence of the third generation of quarks. Moreover, it is a very important mechanism which could have an essential contribution to the asymmetry between matter and antimatter in the Universe. In 1967 A. Sakharov laid out three conditions that would enable a Universe containing initially equal amounts of matter and antimatter to evolve into a matter dominated universe, which we see today [22]. The first condition was a violation of the baryon number conservation B, for which there is still no experimental evidence. However, simple baryon number violation would not be enough to explain matter – antimatter asymmetry if $\mathcal{C}$ and $\mathcal{CP}$ were exact symmetries[1]. As the third condition Sakharov proposed that the Universe should undergo a phase of extremely rapid expansion [22].
Since the first discovery of the $\mathcal{CP}$ – violating neutral kaon decay in 1964, there have been made a big effort to describe the $\mathcal{CP}$ symmetry breaking within the Standard Model. The favoured theoretical framework was provided in 1973 by Kobayashi and Maskawa, who pointed out that $\mathcal{CP}$ violation would follow automatically if there were at least six quark flavours. At present the main experimental effort is focused on the neutral B and D meson system studies [10–13]. However, there are still several interesting open issuses in the kaon physics which, as it will be shown in this chapter, can

[1] In that case there would be a perfect equality between rates of different B violating processes and no asymmetry could be generated from the initially symmetric state [23].

contribute to our better understanding of the $\mathcal{CP}$ violation mechanism.

2.1 The neutral kaon system

Kaons were discovered in 1947 by G. D. Rochester and Clifford C. Butler while studying cosmic ray showers with a cloud chamber [24]. The contrast between the production and decay times of these new particles entailed in 1953 introduction of a new quantum number called „strangeness" S [25, 26]. Strangeness is conserved by both electromagnetic and strong processes while first order weak interaction can induce transitions with $\Delta S = 1$.
Kaons appear in isospin $I = \frac{1}{2}$ doublets: (K^+, K^0) with $S = 1$ and $(\overline{K}^0, K^-)$ with $S = -1$. They can be produced via strong interactions in processes e.g. like:

$$\pi^+ p \to K^+ \overline{K}^0 p$$

$$\pi^- p \to K^0 \Lambda$$

$$p\overline{p} \to K^- \pi^+ K^0$$

$$p\overline{p} \to K^+ \pi^- \overline{K}^0 \ .$$

From the point of view of strong interactions the K^0 meson is a particle with a corresponding antiparticle $\overline{K}^0$. Violation of strangeness conservation by weak interaction allows for transitions like $K^0 \to 2\pi \to \overline{K}^0$ or $K^0 \to 3\pi \to \overline{K}^0$. Thus, the two strangeness eigenstates can oscillate one into another via the $\Delta S = 2$, second order weak interactions, i.e., via virtual 2-pion and 3-pion states. The corresponding quark diagrams for these transitions are presented in Fig. 2.1. Therefore, in the evolution of a kaon in a free space states with well defined mass and width are mixtures of K^0 and $\overline{K}^0$ [27]. The time evolution of the neutral kaon system, which may be given in the K^0 – $\overline{K}^0$ rest frame is determined by Hamiltonian $\mathbf{H}$ and the following equation:

$$i\frac{\partial}{\partial t}\begin{pmatrix} K^0 \\ \overline{K}^0 \end{pmatrix} = \mathbf{H}\begin{pmatrix} K^0 \\ \overline{K}^0 \end{pmatrix} = \left(\mathbf{M} - i\frac{\mathbf{\Gamma}}{2}\right)\begin{pmatrix} K^0 \\ \overline{K}^0 \end{pmatrix} , \tag{2.1}$$

where $\mathbf{M}$ and $\mathbf{\Gamma}$ are 2 x 2 hermitian mass and decay matrices, respectively. In the Weisskopf – Wigner approximation the elements of the mass matrix $\mathbf{M}$ can be expressed as a sum of contributions due to strong and weak interactions [27]:

$$M_{ij} = m_k \delta_{ij} + \langle i|\mathbf{H_W}|j\rangle + \sum_{n \neq K^0, \overline{K}^0} \frac{\langle i|\mathbf{H_W}|n\rangle\langle n|\mathbf{H_W}|j\rangle}{m_K - E_n} , \tag{2.2}$$

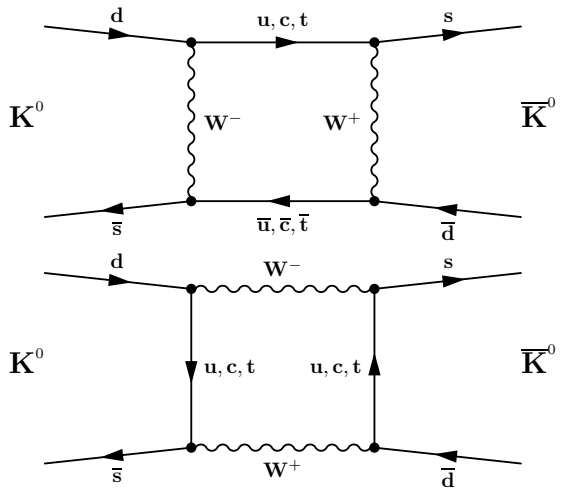


Figure 2.1: Quark diagrams for the K^0 – $\overline{K}^0$ transitions.

where m_K is the neutral kaon mass and $\mathbf{H_W}$ denotes the effective weak Hamiltonian. The sum $\sum_n |n\rangle\langle n|$ runs over all virtual and real states connecting K^0 and $\overline{K^0}$. The decay matrix elements Γ_{ij} related to the kaon decay width by unitarity, originate instead only from $\mathbf{H_W}$ [28]:

$$\Gamma_{ij} = 2\pi \sum_{n \neq K^0, \overline{K}^0} \delta(E_n - m_K) \langle i|\mathbf{H_W}|n\rangle\langle n|\mathbf{H_W}|j\rangle \; . \tag{2.3}$$

If the Hamiltonian of the system is invariant under $\mathcal{T}$, $\mathcal{CP}$ and $\mathcal{CPT}$ M_{ij} and Γ_{ij} have to satisfy the following relations:

$|M_{12} - i\Gamma_{12}/2| = |M_{12}^* - i\Gamma_{12}^*/2|$ ($\mathcal{T}$ conservation),

$|M_{12} - i\Gamma_{12}/2| = |M_{12}^* - i\Gamma_{12}^*/2|$ and $M_{11} = M_{22}, \Gamma_{11} = \Gamma_{22}$ ($\mathcal{CP}$ invariance)

$M_{11} = M_{22}, \Gamma_{11} = \Gamma_{22}$ ($\mathcal{CPT}$ conservation).

Without any assumption about symmetry invariance the Hamiltonian eigenstates of the neutral kaon system seen in nature can be written in the following form [29]:

$$\begin{aligned} |K_S\rangle &= \frac{1}{\sqrt{2(1+|\epsilon_S|)^2}} \left[(1+\epsilon_S)|K^0\rangle + (1-\epsilon_S)|\overline{K}^0\rangle\right] \\ |K_L\rangle &= \frac{1}{\sqrt{2(1+|\epsilon_L|)^2}} \left[(1+\epsilon_L)|K^0\rangle - (1-\epsilon_L)|\overline{K}^0\rangle\right], \end{aligned} \tag{2.4}$$

where ϵ_S and ϵ_L are complex parameters expressing possible $\mathcal{CP}$ and $\mathcal{CPT}$ violation. In particular, if $\mathcal{CPT}$ invariance holds: $\epsilon_S = \epsilon_L = \epsilon$. It is important to stress, that K_S and K_L are kaon states which preserve their identity during the evolution in free space. The experimental values for the lifetimes of these two particles differ by three orders of magnitude. The lifetime of the „short" state $|K_S\rangle$ amounts to

$\tau_S = (8.953 \pm 0.005) \cdot 10^{-11}$ s, while the „long" living particle $|K_L\rangle$ has a lifetime $\tau_L = (5.116 \pm 0.020) \cdot 10^{-8}$ s [19]. This large difference was explained by assuming $\mathcal{CP}$ to be an exact symmetry of the weak interactions. In this case the mass eigenstates defined in Eq. 2.4 reduce to the $\mathcal{CP}$ eigenstates[2] ($\epsilon_L = \epsilon_S = 0$):

$$|K_1\rangle = \frac{1}{\sqrt{2}}\left[|K^0\rangle + |\overline{K}^0\rangle\right] \text{ with } \mathcal{CP} = 1$$
$$|K_2\rangle = \frac{1}{\sqrt{2}}\left[|K^0\rangle - |\overline{K}^0\rangle\right] \text{ with } \mathcal{CP} = -1. \tag{2.5}$$

Neutral kaons decay mainly to the two – and three – pion final states with a well defined $\mathcal{CP}$ eigenvalues [30]:

$$\mathcal{CP}|\pi^+\pi^-\rangle = |\pi^+\pi^-\rangle$$

$$\mathcal{CP}|\pi^0\pi^0\rangle = |\pi^0\pi^0\rangle$$

$$\mathcal{CP}|\pi^+\pi^-\pi^0\rangle = (-1)^{l+1}|\pi^+\pi^-\pi^0\rangle$$

$$\mathcal{CP}|\pi^0\pi^0\pi^0\rangle = -|\pi^0\pi^0\pi^0\rangle\ .$$

For the $|\pi^+\pi^-\pi^0\rangle$ final state the eigenvalue depends on the total angular momentum l. However, since the three pions from the kaon decay are mainly in the relative s – wave state we can assume with a good approximation that the (π^+, π^-, π^0) system is $\mathcal{CP}$ – odd. Thus, $\mathcal{CP}$ conservation would imply that $|K_1\rangle$ state is allowed to decay only to two pions while the „long" living $|K_2\rangle$ decays only to three pions state. Moreover, the large phase space difference between these two decay modes manifests itself in the difference between observed lifetimes.
However, as it is presented in the next section, the $\mathcal{CP}$ invariance is violated by the weak interaction which entails big consequences for the whole particle physics and cosmology.

2.2 $\mathcal{CP}$ violation in kaon decays

In 1964 an experiment by Christenson, Cronin, Fitch and Turlay, unexpectedly exhibited that the long – lived kaon can decay also to the two – pion final states with branching ratio of about $2 \cdot 10^{-3}$ [4]. Thus, the neutral kaons states seen in nature are not $\mathcal{CP}$ eigenstates defined in Eq. 2.5. However, they still can be expressed in the ($|K_1\rangle$,

[2] Here we assume a phase convention where $\mathcal{CP}|K^0\rangle = |\overline{K^0}\rangle$ and $\mathcal{CP}|\overline{K^0}\rangle = |K^0\rangle$ [29].

$|K_2\rangle$) basis:

$$|K_L\rangle = \frac{1}{\sqrt{1+|\epsilon|^2}}\left(|K_2\rangle + \epsilon|K_1\rangle\right)$$
$$|K_S\rangle = \frac{1}{\sqrt{1+|\epsilon|^2}}\left(|K_1\rangle - \epsilon|K_2\rangle\right) \ . \tag{2.6}$$

Since up to now there is no signs of the $\mathcal{CPT}$ symmetry violation from now on we assume [3] $\epsilon_S = \epsilon_L = \epsilon$.

We can understand the $\mathcal{CP}$ symmetry breaking within the scope of two distinct mechanisms referred to as „direct" and „indirect" breaking. The „indirect" violation corresponds to the statement that the true eigenstates of both the strong and electroweak interactions are not exactly $\mathcal{CP}$ eigenstates but have small admixtures of the state with opposite $\mathcal{CP}$ [30]. It is also possible that $\mathcal{CP}$ violation occurs „directly" in the weak decays themselves. In the following the „direct" violation will be explained on the example of kaon decays to two pions. The two – pion systems originating from decays of kaons can be produced with isospin $I = 0$ or $I = 2$ (isospin equal one is forbidden by Bose symmetry [30]):

$$|\pi^0\pi^0\rangle = \sqrt{\frac{1}{3}}|\pi^0\pi^0; I=0\rangle - \sqrt{\frac{2}{3}}|\pi^0\pi^0; I=2\rangle$$
$$|\pi^+\pi^-\rangle = \sqrt{\frac{2}{3}}|\pi^+\pi^-; I=0\rangle + \sqrt{\frac{1}{3}}|\pi^+\pi^-; I=2\rangle.$$

The corresponding weak decay amplitudes of kaons can be expressed as [28]:

$$\langle\pi\pi; I|\mathbf{H_W}|K^0\rangle = A_I e^{i\delta_I}$$
$$\langle\pi\pi; I|\mathbf{H_W}|\overline{K^0}\rangle = A_I^* e^{i\delta_I},$$

where we have explicitly exhibited the final state phases δ_I, which arise from the final state strong interactions of the pions. Direct $\mathcal{CP}$ violation, occurring at the decay vertices, appears as a phase difference between the A_0 and A_2 amplitudes[4] [28]. This phase difference is generated by a class of so called „pengiun" diagrams for s quark decay, one of which is presented in Fig. 2.2.

Typically the $\mathcal{CP}$ violation in the neutral kaon sector is characterized in terms of the following parameters:

$$\eta_{+-} = \frac{A(K_L \to \pi^+\pi^-)}{A(K_S \to \pi^+\pi^-)} = |\eta_{+-}|e^{\phi_{+-}} \cong \epsilon + \epsilon'$$
$$\eta_{00} = \frac{A(K_L \to \pi^0\pi^0)}{A(K_S \to \pi^0\pi^0)} = |\eta_{00}|e^{\phi_{00}} \cong \epsilon - 2\epsilon', \tag{2.7}$$

[3] Although there are some theoretical predictions for the $\mathcal{CPT}$ violation [31–34], all the tests done so far resulted in the confirmation that it is an exact symmetry [19, 35–38].

[4] In general A_0 and A_2 could be real if $\mathcal{CP}$ would be conserved.

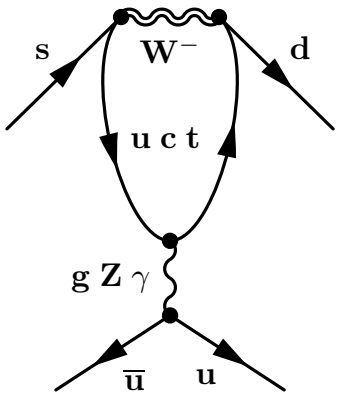


Figure 2.2: „Pengiun" diagram for the s quark decay.

where ϵ is the mixing parameter defined before in Eq. 2.6 and $\epsilon^{'}$ accounts for the direct $\mathcal{CP}$ violation and can be expressed in terms of the weak amplitudes [28]:

$$\begin{aligned}\epsilon' &= \frac{\langle\pi\pi;0|\mathbf{H_W}|K_S\rangle\langle\pi\pi;2|\mathbf{H_W}|K_L\rangle - \langle\pi\pi;0|\mathbf{H_W}|K_L\rangle\langle\pi\pi;2|\mathbf{H_W}|K_S\rangle}{\sqrt{2}\langle\pi\pi;0|\mathbf{H_W}|K_S\rangle^2} \\ &\approx i\frac{e^{i(\delta_2-\delta_0)}}{\sqrt{2}} Im\left(\frac{A_2}{A_0}\right). \end{aligned} \tag{2.8}$$

Above defined parameters were measured many times and are known with a good precision [19]:

$$\begin{aligned} |\eta_{+-}| &= (2.232 \pm 0.011)\cdot 10^{-3}; & \phi_{+-} &= (43.51 \pm 0.05)^\circ \\ |\eta_{00}| &= (2.221 \pm 0.011)\cdot 10^{-3}; & \phi_{00} &= (43.52 \pm 0.05)^\circ \\ |\epsilon| &= (2.228 \pm 0.011)\cdot 10^{-3}; & \phi_{\epsilon} &= (43.51 \pm 0.05)^\circ. \end{aligned} \tag{2.9}$$

Moreover, measurements of the double ratio of the two pion decay rates $|\eta_{+-}|/|\eta_{00}|$ have proved that ϵ' is different from zero indicating occurrence of the direct $\mathcal{CP}$ violation [38].

Analogous $\mathcal{CP}$ invariance breaking should appear also in the K_S decays. As before we can define the following amplitude ratios;

$$\eta_{+-0} = \frac{A(K_S \to \pi^+\pi^-\pi^0)}{A(K_L \to \pi^+\pi^-\pi^0)} = |\eta_{+-0}|e^{\phi_{+-0}} \cong \epsilon + \epsilon'_{+-0} \tag{2.10}$$

$$\eta_{000} = \frac{A(K_S \to \pi^0\pi^0\pi^0)}{A(K_L \to \pi^0\pi^0\pi^0)} = |\eta_{000}|e^{\phi_{000}} \cong \epsilon + \epsilon'_{000}\,. \tag{2.11}$$

As in the case of two – pion decays the ratios contain direct $\mathcal{CP}$ violation parameters related in the lowest order of the Chiral Perturbation Theory by the following equations: $\epsilon'_{+-0} = \epsilon'_{000} = -2\epsilon'$ [39]. The possible $|\pi^+\pi^-\pi^0\rangle$ final state originating from the neutral kaon decays can be produced with isospin $I = 0, 1, 2,$ or 3. The $I = 0$

and $I = 2$ states have $\mathcal{CP} = 1$, and K_S can decay into them without violation of the $\mathcal{CP}$ symmetry. However, they are expected to be strongly suppressed by centrifugal barrier effects [19]. For the $I = 1$ and $I = 3$ states there is no centrifugal barrier and $\mathcal{CP} = -1$ so K_S decay requires violation of this symmetry. Anyhow the two kinds of final states can be separated by the analysis of the $\pi^+\pi^-\pi^0$ Dalitz plot [19]. In the case of $|\pi^0\pi^0\pi^0\rangle$ final state, only isospin $I = 1$ or $I = 3$ is allowed, for which $\mathcal{CP} = -1$. Therefore, the $K_S \to 3\pi^0$ decay is a purely $\mathcal{CP}$ violating process [19].
The present knowledge about η_{+-0} and η_{000} is poor mainly due to very low decay rates for the $K_S \to 3\pi$ decays. The current value of the $K_S \to \pi^+\pi^-\pi^0$ branching ratio amounts to $BR(K_S \to \pi^+\pi^-\pi^0) = (3.5^{+1.1}_{-0.9}) \cdot 10^{-7}$, and the $K_S \to 3\pi^0$ has been never observed [19]. The best upper limit on this decay branching ratio was set by KLOE collaboration and amounts to $BR(K_S \to 3\pi^0) < 1.2 \cdot 10^{-7}$ [16], while the prediction based on Standard Model is equal to about $2 \cdot 10^{-9}$ [39]. The corresponding knowledge about the amplitude ratios can be summarized as follows [19]:

$$\begin{aligned} Re(\eta_{+-0}) &= -0.002 \pm 0.007^{+0.004}_{-0.001} \\ Im(\eta_{+-0}) &= -0.002 \pm 0.009 \\ Im(\eta_{000}) &= -0.001 \pm 0.016 \\ |\eta_{000}| &< 0.018. \end{aligned}$$

Therefore, it is clear, that the full understanding of the $\mathcal{CP}$ violation in the neutral kaon system demands new high statistics measurements, in particular of the $K_S \to 3\pi^0$ decay which is a subject of this work. One of the high precision experiments, which has been greatly contributed to this quest, is the KLOE detection setup which will be presented in the next chapter.

Chapter 3

The KLOE experiment at DAΦNE

In this chapter the characteristics of the DAΦNE collider and the KLOE detector are briefly described. More detailed description can be found in Ref. [20, 40–44].

3.1 The DAΦNE Collider

DAΦNE is an e^+e^- collider, optimized to work with a center of mass energy around the ϕ mass, $M_\phi = (1019.418 \pm 0.008)$ MeV [43]. The „heart" of the collider are two storage rings in which 120 bunches of both, electrons and positrons, are stored. Each bunch collides with its counterpart once per turn, minimizing the mutual perturbations of colliding beams. Electrons are accelerated to final energy in the Linac (see Fig. 3.1),

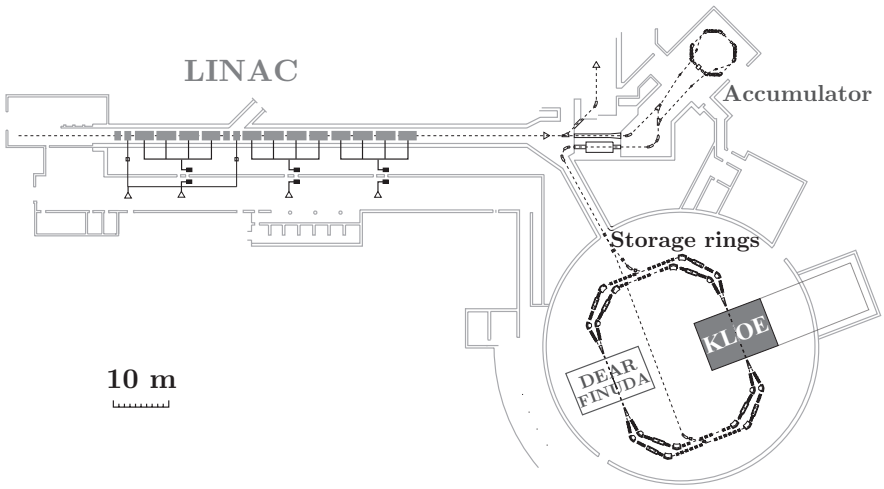


Figure 3.1: Schematic view of the DAΦNE collider. The picture was adapted from [20].

accumulated and cooled in the accumulator and transferred to a single bunch in the ring [20]. Positrons are created in an intermediate station in the Linac, and then follow the same procedure as electrons. Both, electrons and positrons are injected into the

rings at final energy of about 510 MeV. The beams collide in two interactions regions, with a frequency up to 356 MHz, corresponding to a minimum bunch crossing period of $T_{rf} = 2.7$ ns. The e^+e^- collisions result in ϕ meson creation which is almost at rest ($\beta_\phi \approx 0.015$) and decay predominantly to K^+K^- (49%), K_SK_L (34%), $\rho\pi$ (15%) and $\eta\gamma$ (1.3%) final states [19]. The decay products are registered using the KLOE detection setup, which consists of large cylindrical drift chamber surrounded by the electromagnetic calorimeter. The components of KLOE will be briefly described in the next section.

3.2 The KLOE detector

The KLOE detector consists of a large cylindrical drift chamber and a hermetic electromagnetic calorimeter. A superconducting coil and an iron yoke (see Fig. 3.2) surrounding the calorimeter provides a 0.52 T magnetic field. The beam pipe at the interaction region is a beryllium sphere with 10 cm of radius and 0.5 mm thick. This structure minimizes both the multiple scattering and the energy loss of the charged particles from K_S decays, as well as the probability of K_L regeneration [43].

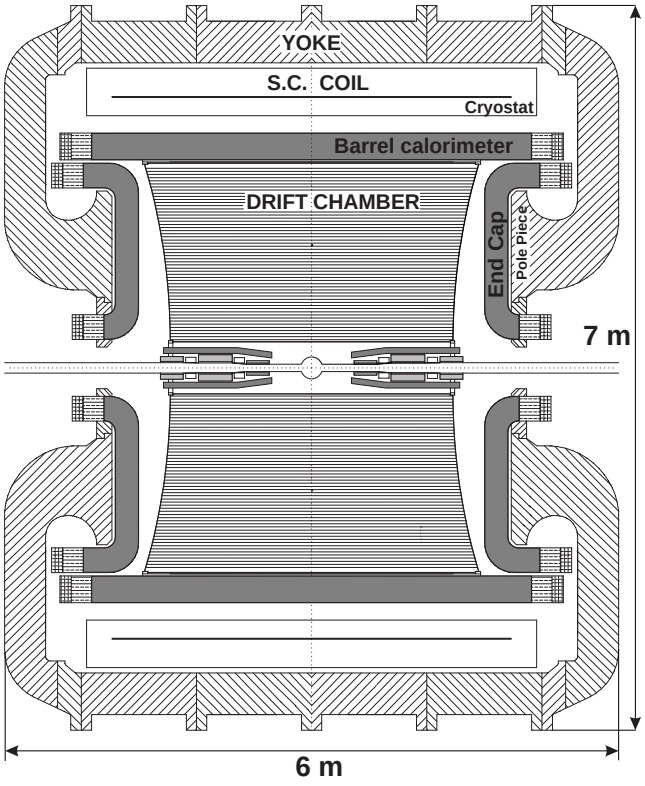


Figure 3.2: Vertical cross section of the KLOE detector. The figure is adapted from [20].

3.2.1 The Drift Chamber

The KLOE drift chamber has a cylindrical shape 3.3 m long, with internal and external radii of 25 cm and 2 m, respectively [43]. It was designed to register all charged secondary products from the K_L decay and measure their properties with great precision [20]. Thus, its size was dictated by a long lifetime of this particle[1]. To minimize the K_L regeneration, multiple Coulomb scattering and photon absorption KLOE drift chamber is constructed out of carbon fiber composite with low-Z and low density, and uses a gas mixture of helium (90%) and isobutane (10%) [21]. The radiation length of the gas amounts to about 900 m, including the contribution of the 52140 wires [43]. In order to obtain high and uniform track and vertex reconstruction efficiencies, wires are strung in an all – stereo geometry, with stereo angles varying with the radius from 50 mrad to 120 mrad going outward [43]. This design results in a uniform filling of the sensitive volume with almost square drift cells, with shape slowly changing along z axis[2]. Fig. 3.3 shows the wire geometry during the drift chamber construction as illuminated by light. Particles from the ϕ decays are produced with small momenta and therefore track density is much higher at small radii [43]. Thus, dimensions of the cells were designed to be of about 2 x 2 cm^2 for the 12 innermost wire layers, and to of about 3 x 3 cm^2 for the remaining 48 layers [42].

To extract the space position from the measured drift time of the incident particle, 232 space – to – time relations are used. They are parametrized in terms of two angles β and $\widetilde{\phi}$ defined in Fig. 3.4. The β angle characterizes the geometry of the cell directly related to the electric field responsible for the avalanche multiplication mechanism. $\widetilde{\phi}$ instead gives the orientation of the particle trajectory in the cell's reference frame, defined in the transverse plane and with origin in the sense wire of the cell [20].

Using the wire geometry, space – to – time relations and known magnetic field one can reconstruct the tracks and vertices of charged particles. The reconstruction procedure starts with pattern recognition and is followed by track and vertex fitting. The pattern recognition associates hits[3] close in space to form track candidates and gives a first estimate of the track parameters. Then track fitting provides the final values of these parameters by minimization procedure based on the difference between the fitted and the expected drift distances (so called residuals), as evaluated from measured drift times and space – to – time relations. Finally the vertex fit procedures search for possible primary and secondary vertices, on the basis of the distance of closest approach between tracks [20].

To ensure the stability in time of the KLOE drift chamber performance, the system

[1] The mean decay path of the K_L meson produced in the ϕ decay amounts to about 3.4 m [20].

[2] The z axis of the KLOE reference frame is defined as the bisector of the angle between colliding e^+ and e^- beams [20].

[3] As a hit we consider a presence of a signal on a sense wire.

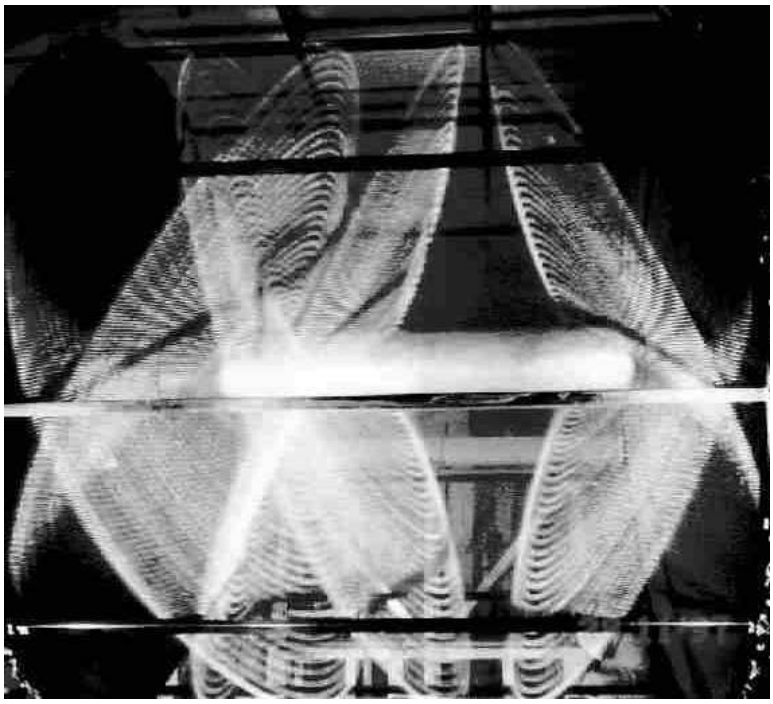


Figure 3.3: Drift chamber stereo wires geometry. The figure is adapted from [45].

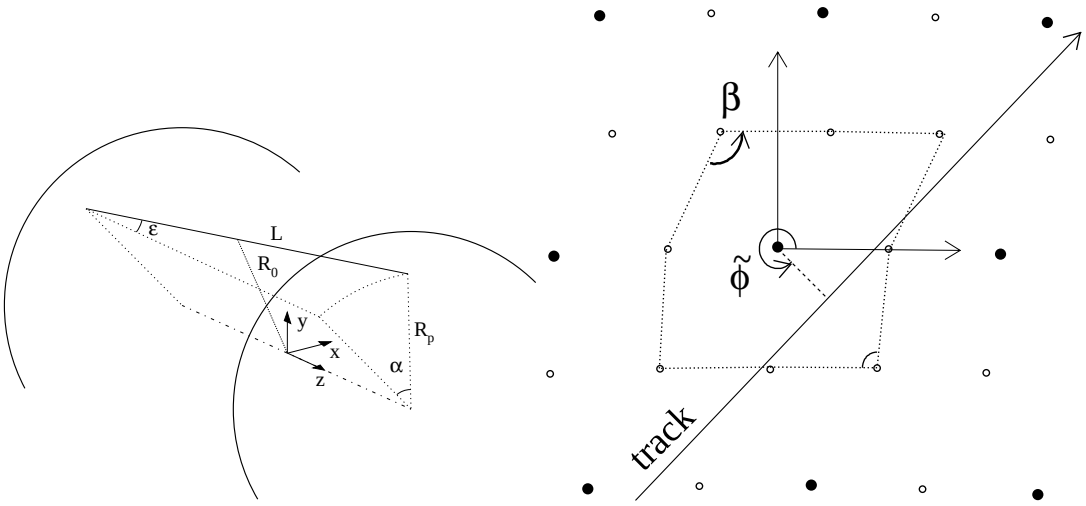


Figure 3.4: Left: Wire geometry with the definition of stereo angle ϵ between the wire of length L and the z – axis. Right: Definition of β and $\widetilde{\phi}$ angles characterizing the shape of the cell and the angle of the incident track [20]. The figures are adapted from [20].

is calibrated periodically by acquiring samples of cosmic ray events suitable for the measurement of about 200 different space – to – time relations [20]. The calibration is performed at the beginning of each KLOE run and selects about 80000 cosmic ray events [42]. These events are tracked using the existing space – to – time relations and the average value of the residuals for hits in the central part of the cells is monitored. If the residuals exceed 40 μm additional $3{\cdot}10^5$ cosmic ray events are collected, and a new set of calibration constants is obtained. Finally, during data taking the drift chamber performances are monitored using selected samples of events [42].
The KLOE drift chamber provides tracking in three dimensions with a resolution in the transverse plane of about 200 μm, resolution in the z-coordinate measurement of about 2 mm and of 1 mm on the decay vertex position. The momentum of the particle is determined from the curvature of its trajectory in the magnetic field with a fractional accuracy $\sigma_p/p \; = \; 0.4\%$ for polar angles larger than 45° [20].

3.2.2 The Electromagnetic Calorimeter

The KLOE electromagnetic calorimeter was designed to provide hermetic detection of low energy gamma quanta with high efficiency, good energy resolution and excellent time resolution for the neutral vertex reconstruction and to trigger the events [20]. It consists of a barrel built out of 24 trapezoidal shaped modules and side detectors (so called endcaps) read out from both sides by a set of photomultipliers. The barrel is a cylinder with an inner diameter of 4 m, made of 24 modules 4.3 m long and 23 cm thick. Each endcap consists of 32 vertical C – shaped modules. This structure covers 98% of the full solid angle. Each module consists of a mixture of lead (48% of the volume), scintillating fibers (42%), and glue (10%) [43]. Fibers, each with a diameter of 1 mm, are embedded in 0.5 mm lead foils accelerating the showering processes. The special care in design and assembly of the Pb – fiber composite ensures that the light propagates along the fiber in a single mode with velocity ∼17 cm/ns, which greatly reduces spread of the light arrival time at the fiber ends [20]. Calorimeter modules are read out at both ends viewed by light guides of area of 4.4 x 4.4 cm^2 coupled to the photomultipliers transforming the light into electric impulses. This defines so called „calorimeter cells" which form five larger structures (see Fig. 3.5): planes 4.4 cm wide[4].
When a particle hits the calorimeter for each cell both, the charge as well as time of arrival of the photomultiplier signals are registered. The cell energy is taken as the average of the energy registered at both sides, after correcting for the light attenuation along the fiber [43]. The energy calibration starts by a first equalization in cell response to minimum ionizing particles at calorimeter center, and by determining the attenuation

[4]The last plane of cells is 5.2 cm wide.

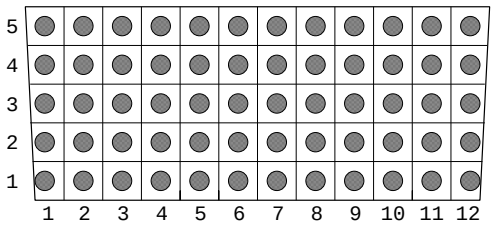


Figure 3.5: Schematic view of the readout structure on one side of the barrel module [46]. 60 defined cells form 5 planes and 12 columns of the calorimeter module. Filled circles represents photomultipliers. The figure is adapted from [46].

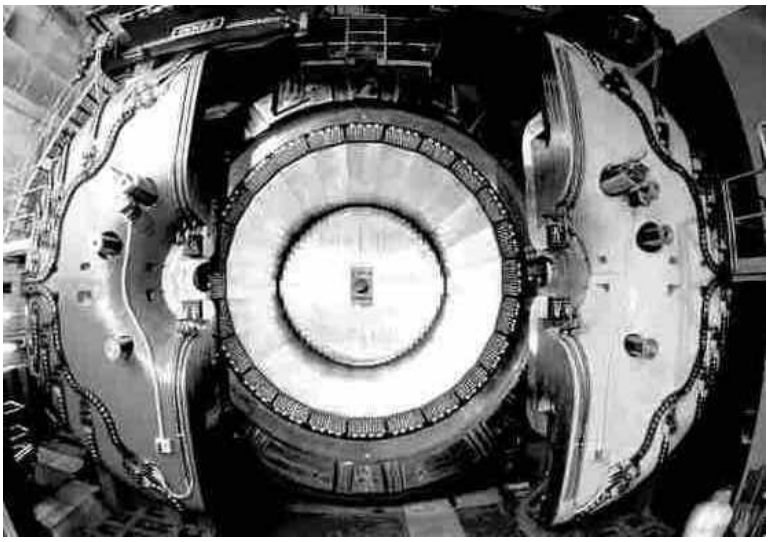


Figure 3.6: Photograph of the KLOE calorimeter. One can see 24 modules of the barrel and the inner plane of one of the endcaps. The figure is adapted from [46].

length of each single cell using cosmic rays acquired in dedicated runs. This is done before the start of each long data taking period [20]. The energy determined from the measured amplitudes of signals for both sides A and B of a cell S^{AB} amounts to:

$$E^{A,B}(\mathrm{MeV}) = \frac{S^{A,B} - S_0^{A,B}}{S_M} \cdot K, \tag{3.1}$$

where $S_0^{A,B}$ are the zero – offsets of the amplitudes scale, S_M corresponds to the response for the minimum ionizing particle crossing the calorimeter center and K factor gives the energy scale in MeV [46]. The total energy deposited in a cell is calculated as the mean of values determined at both ends for each cell. The determination of the absolute energy scale K relies on a monochromatic source of 510 MeV photons: the $e^+e^- \to \gamma\gamma$ sample. The latter calibration is routinely carried out each 200 – 400 nb^{-1} of collected luminosity [20].

For each cell two time signals T^A and T^B (digitized by the Time to Digital Converter TDC) are recorded. The arrival time t and position s of the impact point along the fiber direction can be determined as[5]:

$$t(\mathrm{ns}) = \frac{1}{2}(t^A + t^B - t_0^A - t_0^B) - \frac{L}{2v} \,, \tag{3.2}$$

$$s(\mathrm{cm}) = \frac{v}{2}(t^A - t^B - t_0^A + t_0^B) \,, \tag{3.3}$$

with $t^{A,B} = c^{A,B} \cdot T^{A,B}$, where $c^{A,B}$ are the TDC calibration constants, $t_0^{A,B}$ denotes overall time offsets, L stands for length of the cell (cm) and v is the light velocity in fibers (cm/ns) [40].

Based on the reconstructed energies, times and positions cells are merged into calorimeter clusters. First the adjacent cells are grouped into so called „preclusters"[6]. The time spread of cells forming the precluster has to be smaller than 2.5 ns [46]. Moreover, cells are merged in one cluster if a distance between them and the center of the precluster is less than 20 cm [46]. The cluster energy is evaluated as the sum of the cells energies:

$$E_{cl} = \sum_i E_i \,, \tag{3.4}$$

while the time and position centroids are obtained as weighted averages:

$$T_{cl} = \frac{\sum_i E_i \cdot t_i}{\sum_i E_i} \tag{3.5}$$

$$\mathbf{R_{cl}} = \frac{\sum_i E_i \cdot \mathbf{r_i}}{\sum_i E_i} \,. \tag{3.6}$$

i denotes the ith cell belonging to the cluster and $\mathbf{r_i}$ stands for the cell's position vector with respect to the interaction point. T_{cl} is next related to the time of flight of particle from the interaction point to the cluster position. It is done subtracting the event global time offset, common to all channels and depending on the trigger formation time with respect to the real e^+e^- interaction time. Due to the spread of the particle's arrival times, the KLOE trigger is not able to identify the bunch crossing related to each event, which has to be determined offline [20]. The common „Start" signal to the calorimeter TDC boards is provided by the first level trigger, which will be described in the next section. The „Stop" instead is given by the photomultiplier signals delayed because of the electronics and light propagation in the fibers [43]. Time measured by the calorimeter can be expressed as:

$$T_{cl} = T_{tof} + \delta_c - N_{bc} \cdot T_{rf} \,, \tag{3.7}$$

[5] $s = 0$ is assumed to be at the fiber center.

[6] A cell is added into a precluster only if its times and energies were reconstructed at both sides of the calorimeter module.

where T_{tof} is the time of flight of a particle from the interaction point to the cluster position, δ_c is a single number accounting for the overall electronic offsets and cable delays, and N_{bc} is the number of bunch – crossing periods needed to generate the TDC start. The values of δ_c and N_{bc} are determined for each data taking run with $e^+e^- \to \gamma\gamma$ events by looking at the $\Delta_{TOF} = T_{cl} - R_{cl}/c$ distributions (c denotes the speed of light) [20]. For such events this distribution shows well separated peaks corresponding to different values of N_{bc}. We define δ_c as the position of the largest peak in the distribution, and obtain T_{rf} from the distance between peaks [44]. During offline processing, to allow the cluster times to be related to the particle time of flight, we determine for each event the corrected cluster times:

$$t_{cl} = T_{cl} - (\delta_c - N_{bc} \cdot T_{rf}) \; . \tag{3.8}$$

The KLOE electromagnetic calorimeter allows for measurements of particle energies and flight time with accuracies of $\sigma_E = \frac{5.7\%}{\sqrt{E[\mathrm{GeV}]}} E$ and $\sigma(t) = \frac{57\mathrm{ps}}{\sqrt{E[\mathrm{GeV}]}} \oplus 140$ ps, respectively [40]. Analysis of the signal amplitude distributions allows to determine the location where the particle hits the calorimeter module with accuracy of about 1 cm in the plane transverse to the fiber direction. The longitudinal coordinate precision is energy dependent: $\sigma_z = \frac{1.2 \text{ cm}}{\sqrt{E[\mathrm{GeV}]}}$ [21].

3.2.3 The Trigger system

The KLOE trigger system is based on local energy deposits in the electromagnetic calorimeter and hit multiplicity information from the drift chamber. It has been optimized to retain almost all $e^+e^- \to \phi$ decays, and provide efficient rejection on the two main sources of background: small angle $e^+e^- \to e^+e^-$ scattering and particle lost from the DAΦNE beams [20]. Moreover, all e^+e^- scattering and $\gamma\gamma$ events produced at large polar angles are gathered for detector monitoring and calibration. Since the DAΦNE bunch crossing period amounts to $T_{rf} = 2.7$ ns, KLOE trigger must operate in continuous mode. A two level scheme was chosen. A first level trigger T1 is produced with a minimal delay ($\sim$ 200 ns) and is synchronized with the DAΦNE master clock [41]. The T1 signal initiates conversion in the front – end electronics modules, which are subsequently read out following a fixed time interval of about 2.6 μs. This corresponds to the typical drift time of electrons travelling in the drift chamber cells [20]. After the arrival of a first level trigger, additional information is collected from the drift chamber, which is used together with the calorimeter information as a second level trigger T2. It confirms the first level trigger, initializes digitisation of the drift chamber electronics and starts the data acquisition readout. If no T2 signal arrives before the end of 2.6 μs dead time, all readout is reset [41].

T1 and T2 triggers are based on the topology of energy deposits in the KLOE electromagnetic calorimeter and on the number and spatial distribution of the drift chamber hits. Since ϕ decay events have a relatively high multiplicity, they can be efficiently selected by the calorimeter trigger by requiring two isolated energy deposits above a threshold of 50 MeV in the barrel and 150 MeV in the endcaps. Events with only two fired sectors in the same endcap are rejected, because this topology is dominated by machine background. Moreover, we require about 15 hits in the drift chamber within a time window of 250 ns from beam crossing [20]. The trigger identifies $e^+e^- \to e^+e^-$ events requiring clusters with energy of about 350 MeV. An event which satisfies at least one of the two above conditions and is not recognized as e^+e^- scattering, generates a first level trigger T1[7]. The level – 2 trigger T2, requires further multiplicity or geometrical conditions for the electromagnetic energy deposits, or about 120 drift chamber wire signals within a 1.2 μs time window. At the level 2 trigger recognizes also the cosmic ray events by the presence of two energy deposits above 30 MeV in the outermost calorimeter layers [20]. A fraction about 80$\%$ of the cosmic ray events are identified and rejected at the trigger level with this technique. Further suppression of the DAΦNE background events and cosmic rays is performed by an off – line filter called FILFO (*FILtro FOndo*: background filter). FILFO identifies background events at a very early stage of the data reconstruction using only information from the calorimeter [47].
For the search of the $K_S \to 3\pi^0$ decay only the calorimeter signals are used to trigger the event. Two energy deposits above threshold about 50 MeV for the barrel and about 150 MeV for the endcaps are required [16].

[7] As it was mentioned a part of the $e^+e^- \to e^+e^-$ events are gathered for detector monitoring and calibration.

Chapter 4

First stage of the event selection

The ϕ meson produced in the e^+e^- collision at DAΦNE is in a pure $J^{PC} = 1^{--}$ state. Since the $\phi \to K_S K_L$ decay is driven by the strong interaction, the initial $K_S K_L$ state is antisymmetric with the same quantum numbers and can be written in the ϕ rest frame as:

$$|i\rangle = N \cdot [|K_S(\vec{p})\rangle\,|K_L(-\vec{p})\rangle - |K_L(\vec{p})\rangle\,|K_S(-\vec{p})\rangle] \ , \tag{4.1}$$

where $\vec{p}$ denotes the momentum of each kaon and N is a normalization factor [35]. Since the ϕ resonance is moving with a small momentum in the horizontal plane $P_\phi \approx 13\ \mathrm{MeV/c}$ K_S and K_L mesons are produced almost back – to – back in the laboratory frame. Therefore, observation of a K_L (K_S) decay ensures the presence of a K_S (K_L) meson travelling in the opposite direction[1] [48]. Thus, at DAΦNE we obtain pure K_S and K_L „beams" with precisely known momenta and flux, which can be used to measure absolute branching ratios [20]. In this chapter the K_S tagging technique with the detection of the K_L interaction in the KLOE calorimeter is described.

4.1 Identification of K_S via detection of K_L

Neutral kaons produced at KLOE have a velocity in the ϕ rest frame equal to $\beta \approx 0.22$. This corresponds to the K_L time of flight from the interaction point to the calorimeter equal to about 31 ns, which means that about 60% of produced K_L mesons reach the calorimeter without decaying [20]. K_L mesons interact in the calorimeter with an energy release up to $\sim$ 497 MeV (so called „K_L – crash"). Thanks to the exceptional timing capabilities of the KLOE calorimeter[2] and the low velocity of kaons one can use the Time of Flight technique to tag the K_S meson, as described in the next section.

[1] We refer to the process of defining a K_S or K_L sample as tagging: observation of a K_L (K_S) decay tags the presence of a K_S (K_L) meson and allows for the determination of its momentum [48].

[2] For an energy release of 100 MeV the resolution of time measured by the calorimeter amounts to about 0.3 ns, which corresponds to about 1% accuracy in the determination of the K_L velocity [20].

Adding the information about the position of the energy release (K_L cluster), the direction of the K_L flight path can be determined with $\sim 1^\circ$ angular accuracy [20]. This allows to estimate the K_L momentum vector and as a consequence, knowing the ϕ four – momentum, to determine the four – momentum of the tagged K_S meson.

4.1.1 Identification of the K_L meson

The identification of the K_L interaction in the calorimeter is performed after tracks reconstruction and association to the clusters[3], and after the preselection aiming at the rejection of events with K_L meson decay inside the drift chamber. Events for which there is one reconstructed vertex with two tracks having opposite curvature are rejected. Moreover, an event is discarded if there are two reconstructed tracks, having opposite curvature, associated to two vertices reconstructed less than 30 cm away from the interaction point in the transverse plane. These cuts reject most of the background events with K_L decaying before reaching the calorimeter [49]. For each surviving event we look for the K_L clusters in the calorimeter taking into account only clusters not associated to any track. For each that kind of clusters we calculate velocity of the contributing particle defined in the laboratory frame as:

$$\beta_{cl} = \frac{R_{cl}}{c \cdot t_{cl}} \,, \tag{4.2}$$

where R_{cl} denotes the distance from the e^+e^- interaction point to the reconstructed position of the cluster center, t_{cl} stands for the measured time of flight of the particle and c is the speed of light. Since in the ϕ rest frame kaons have a well known velocity $\beta \approx 0.22$ it is convenient to transform β_{cl} to this reference frame:

$$\beta_{cr} = \frac{\sqrt{\beta_\phi^2 + \beta_{cl}^2 + 2\beta_\phi\beta_{cl}\cos\alpha}}{1 + \beta_\phi\beta_{cl}\cos\alpha} \,, \tag{4.3}$$

where β_ϕ denotes the velocity of the ϕ meson in the laboratory frame and α stands for the angle between the ϕ momentum vector and a direction vector connecting the interaction point with the cluster position. The distribution of β_{cr} is presented in Fig. 4.1a. A big peak around $\beta_{cr} = 1$ corresponds mainly to clusters formed by gamma quanta from K_S mesons which decay very close to the interaction point. Clusters originating from the decay products of remaining K_L decays are instead characterized by smaller velocities distributed in the range from $\beta_{cr} \approx 0.28$ to $\beta_{cr} \approx 1$ [49]. In Fig. 4.1a one can also see a structure around $\beta_{cr} \approx 0.22$ corresponding to K_L mesons and a smaller peak for very low velocities. The latter peak originates mainly from the charged particles

[3] The track – to – cluster association procedure establishes correspondence between tracks in the drift chamber and clusters in the calorimeter.

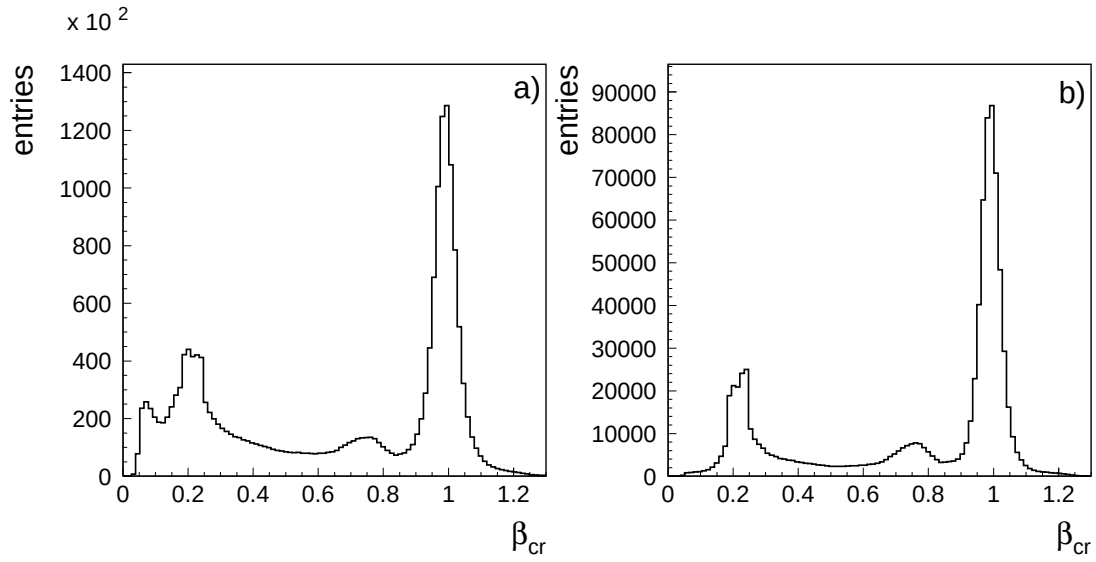


Figure 4.1: Distribution of the β_{cr} velocity reconstructed for clusters not associated to the track for a sample of events before identification of the K_L interaction in the calorimeter. The spectra are made for all clusters before (a) and after (b) cut on energy $E_{cr} > 100$ MeV.

(e.g. pions) for which the track – to – cluster association procedure failed. Additionally, most of these clusters are characterized by energy deposits smaller than 100 MeV [49]. The β_{cr} distribution after the cut on $E_{cr} > 100$ MeV is shown in Fig. 4.1b, where one can see a big suppression of the clusters with lowest velocity. Therefore, clusters originating from the K_L interaction in the calorimeter are defined with the following conditions:

$$\begin{aligned} 0.17 < \beta_{cr} < 0.28 \\ E_{cr} > 100 \text{ MeV} , \end{aligned} \tag{4.4}$$

where E_{cr} is the energy of the K_L cluster.
The main remaining background sources to this tagging algorithm are the cosmic muons entering KLOE through the intersection between the barrel and endcap calorimeters. Such muons may give a signal in the calorimeter without a track in the KLOE drift chamber. The other contributions to the background originate from DAΦNE activity and $\phi \to K^+K^-$ decays [43]. The angular momentum of the K_LK_S system is equal to the spin of the ϕ meson $s = 1$. Therefore, kaons from the ϕ decay are mostly emitted in the direction perpendicular to the beam axis and the background can be additionally suppressed selecting only „K_L – crash" clusters in the barrel [43].
K_L meson interacting in the calorimeter usually induces more than one cluster, therefore to estimate the direction of the tagging K_L meson we consider the „fastest" candidate cluster which was produced as the first one.

4.1.2 K_L – momentum estimate

In the $\phi \to K_S K_L$ decay the K_L four – momentum $\mathbb{P}_{\mathbb{K}_\mathbb{L}}$ can be determined completely knowing the center of mass energy $\sqrt{s}$, the ϕ momentum P_ϕ vector and α angle between the ϕ momentum and the K_L flight direction determined in the laboratory frame from the reconstructed center of the cluster. For $\sqrt{s}$ and P_ϕ we use the mean values measured for each running period using the gathered sample of e^+e^- scattered at large angles. Determination of $\mathbb{P}_{\mathbb{K}_\mathbb{L}}$ allows to calculate the four – momentum of the tagged K_S meson: $\mathbb{P}_{\mathbb{K}_\mathbb{S}} = \mathbb{P}_\phi - \mathbb{P}_{\mathbb{K}_\mathbb{L}}$.

Chapter 5

Normalization sample

Registration of the K_L interactions in the calorimeter allows for the simultaneous identification of the K_S meson. Since one of the goals of this measurement is to determine the $K_S \to 3\pi^0$ decay branching ratio, the number of events selected as the signal has to be normalized to the number of all K_S decays. To this end the $K_S \to 2\pi^0 \to 4\gamma$ events were also counted (further on they will be referred to as the normalization sample). This process is one of the main K_S decay channel with well – known branching ratio $BR(K_S \to 2\pi^0) = 0.3069 \pm 0.0005$ [19]. The number of events produced for both the signal and the normalization sample can be expressed as:

$$\begin{aligned} N_{2\pi} &= L \cdot \sigma_\phi \cdot BR(\phi \to K_S K_L) \cdot BR(K_S \to 2\pi^0) \cdot \epsilon_{2\pi} \cdot \epsilon_{cr} \\ N_{3\pi} &= L \cdot \sigma_\phi \cdot BR(\phi \to K_S K_L) \cdot BR(K_S \to 3\pi^0) \cdot \epsilon_{3\pi} \cdot \epsilon_{cr} \ , \end{aligned} \tag{5.1}$$

where L is the integrated luminosity, σ_ϕ denotes the total cross section for ϕ production, ϵ_{cr} stands for the tagging efficiency and $\epsilon_{3\pi}$ and $\epsilon_{2\pi}$ are the identification efficiencies for the appropriate channel. The ratio:

$$\frac{N_{3\pi}}{N_{2\pi}} = \frac{BR(K_S \to 3\pi^0) \cdot \epsilon_{3\pi}}{BR(K_S \to 2\pi^0) \cdot \epsilon_{2\pi}} \tag{5.2}$$

allows for the $BR(K_S \to 3\pi^0)$ determination independently of L, σ_ϕ, ϵ_{cr} and the $\phi \to K_S K_L$ branching fraction avoiding all the systematic effects originating from measurements of these quantities.

After identification of the K_L meson interacting in the calorimeter the preselection is based on the number of reconstructed γ quanta in each event. To this end we consider only calorimeter clusters not associated to any track reconstructed in the drift chamber. Moreover, the reconstructed time of the cluster t_{cl} should be compatible with the time of flight of photon equal to R_{cl}/c, where R_{cl} is the distance from the cluster position to the interaction point[1] and c denotes the speed of light. We assume the two times to

[1] Since the mean free path of the K_S originating from the ϕ decay amounts to about 6 mm (the kaon velocity $\beta \sim 0.215$) , which corresponds to negligible time delay equal to $\sim$ 100 ps, we assume that it

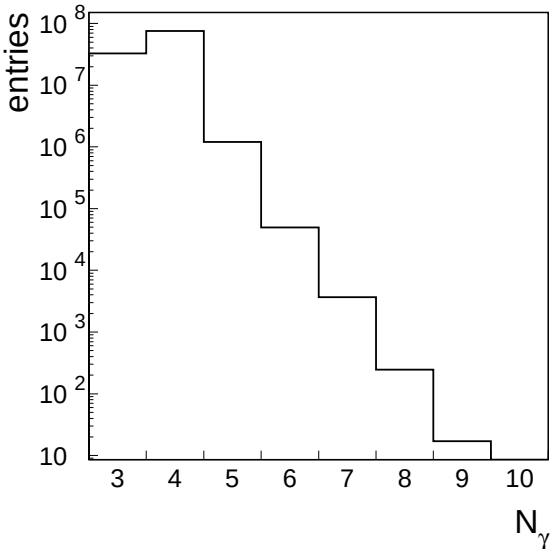


Figure 5.1: The experimental distribution of the reconstructed γ quanta multiplicities after imposing the tight K_S tag requirements ($E_{cr} > 150\,\mathrm{MeV}$ and $0.200 < \beta_{cr} < 0.225$) and acceptance cuts defined by Eqs. 5.3, 5.5 and 5.6.

be consistent if:

$$|t_{cl} - R_{cl}/c| \leq \mathrm{MIN}(3.5 \cdot \sigma_t(E_{cl}), 2\,\mathrm{ns})\,, \tag{5.3}$$

where σ_t is the calorimeter time resolution parametrized as a function of the cluster energy E_{cl}:

$$\sigma_t(E_{cl}) \;=\; \frac{57\,\mathrm{ps}}{\sqrt{E_{cl}(\mathrm{GeV})}} \;\oplus\; 140\,\mathrm{ps}\,. \tag{5.4}$$

The cutoff on 2 ns is used to reduce the number of the machine background clusters accidentally overlapping with the event. To this end we apply also cuts on the minimal cluster energy and polar angle:

$$E_{cl} > 7\,\mathrm{MeV} \tag{5.5}$$

$$|\cos(\theta_{cl})| \leq 0.915 \iff 23.8^\circ \leq \theta_{cl} \leq 156.2^\circ\,. \tag{5.6}$$

Distribution of the γ quanta multiplicities is shown in Fig. 5.1. At this stage of analysis we select two data subsets: the signal sample which consists of events with six reconstructed photons and the normalization sample of $K_S \to 2\pi^0$ candidates with N_γ = 4. For both channels the expected background as well as the detector acceptance and the analysis efficiency is estimated using the Monte Carlo simulations based on the GEANT3 package [50]. The simulations incorporate a detailed geometry and material composition of the KLOE apparatus and all the conditions of the experiment e.g.

decays exactly in the interaction point.

DAΦNE background rates, position of the interaction point and beam parameters[2].

5.1 Comparison between data and simulations results for 4γ events

For the search of rare processes like the $K_S \to 3\pi^0$ the estimation of the background has to be as precise as possible. In our research to this end we use Monte Carlo simulations described briefly in the introduction to this chapter. Moreover, the determination of the efficiencies of cuts and discriminant analysis is also based on the simulated samples of events. Therefore, we have checked the reliability of the KLOE Monte Carlo simulations and optimized them for the best possible description of the experimental data.

Since the reconstruction efficiency of clusters in the calorimeter is slightly higher for simulations compared to the measured data we apply a correction determined based on the $\phi \to \pi^+\pi^-\pi^0$ sample[3]. The efficiency for both data and simulations were parametrized as a function of the γ quanta energy and polar angle. The correction is then applied deleting randomly photons from the simulated events with a probability equal to the ratio of efficiencies for data and simulations [51, 52].

Apart from the cluster reconstruction efficiency the simulations were corrected also for the energy scale of the reconstructed gamma quanta. The necessity of this additional correction is justified in Fig. 5.2a where we observe a small shift between the distributions of the reconstructed K_S mass for data and simulations before the correction. The procedure of the energy scale correction for Monte Carlo events is based on the $K_S \to 2\pi^0 \to 4\gamma$ sample which is almost background free. For both, data and simulations the following variable has been constructed:

$$\Delta E_\gamma = \frac{E_\gamma - E_{fit}}{E_{fit}} \,, \tag{5.7}$$

where E_γ is the energy of reconstructed gamma quantum and E_{fit} denotes energy of the same gamma quantum corrected by the kinematical fit procedure. The gamma quanta were then divided into groups of 20 MeV with respect to the E_{fit}. For each group the ΔE_γ distribution was fitted with the Gauss function. The mean values of the fitted Gauss distributions are shown in Fig. 5.3a. As it can be seen Monte Carlo simulations systematically underestimate the data. The energy scale correction was applied by increasing the cluster energies by a factor parametrized as a function of E_{fit}. For

[2]The detailed description of the KLOE Monte Carlo simulation program GEANFI can be found in Ref. [44].

[3]The detailed description of the cluster reconstruction efficiency studies for data and simulations can be found in Ref. [52].

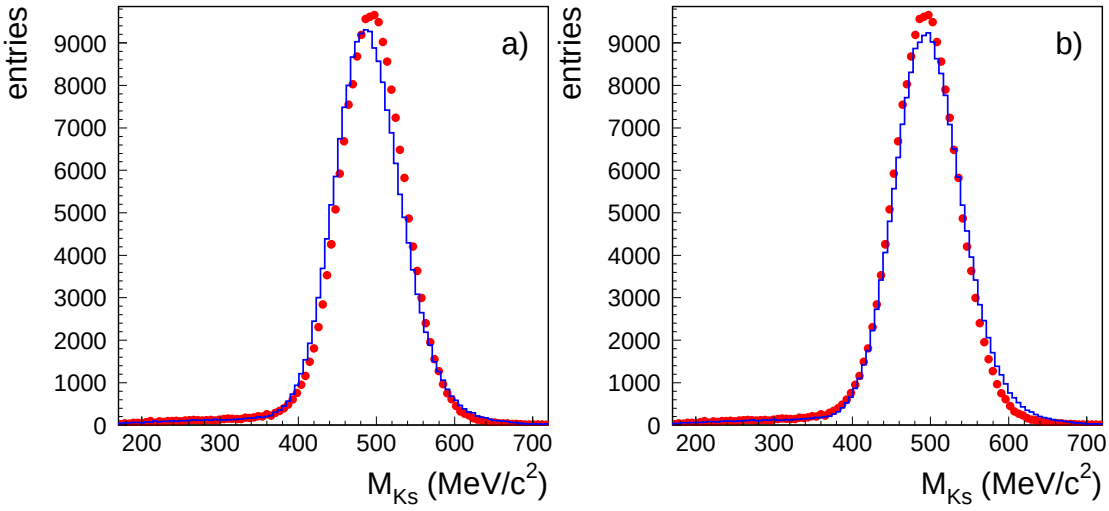


Figure 5.2: Comparison between the reconstructed K_S mass distributions for data (red points) and simulations (blue histogram) before a) and after b) the energy scale correction. The K_S mass is reconstructed from the $K_S \to 2\pi^0$ events.

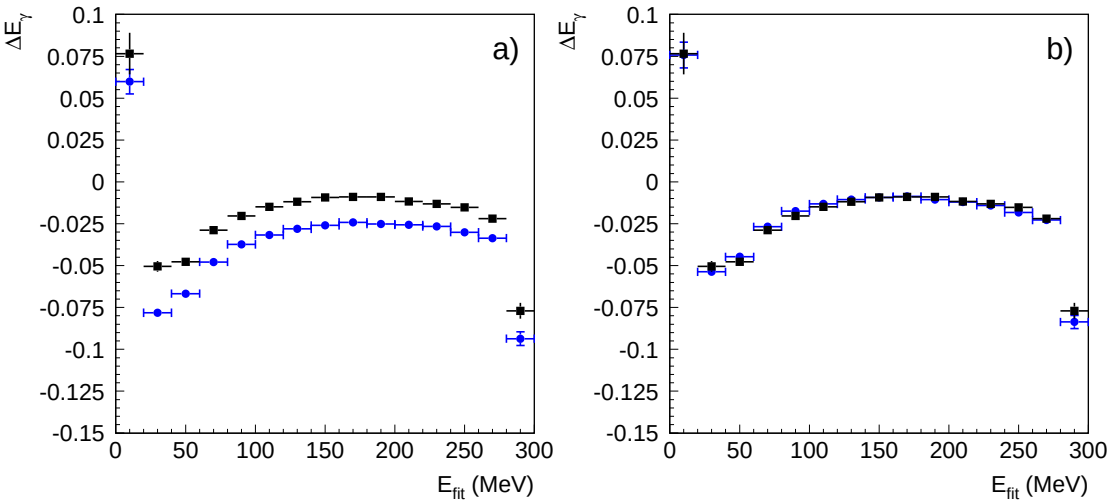


Figure 5.3: Distributions of the mean ΔE_γ for data (black squares) and simulations (blue circles) without energy scale correction a) and after the correction b). The values are obtained using the fit described in the text.

the first 20 MeV bin we started with 2.4% shift while for every next group of clusters the correction was decreasing by a factor of 0.1%. The result is presented in Figs. 5.2b and 5.3b where one can see much better agreement with the data.
For further validation and tuning of the simulations, after applying the cluster efficiency correction, we have determined relative fractions of number of events with given γ quanta multiplicity k with respect to the total number of events with 3 – 6 reconstructed photons:

$$F_k = \frac{N_{ev}(k)}{\sum_{i=3}^{6} N_{ev}(i)} \ , \tag{5.8}$$

and compared experimental values of F_k with results of simulations. The distributions of the relative fractions as a function of the KLOE running period are presented in Fig. 5.4. The agreement between data and simulations is reasonable apart from the most important multiplicity F_6 where results of the simulations systematically overestimate the data during the whole data taking period. To understand the source of this discrepancy we have determined the probabilities to find one (P_{A1}) or two (P_{A2}) accidental clusters in the prompt time window defined in Eq. 5.3 for both data and simulations. To this end we have considered clusters in so called early time window i.e. background clusters originating from earlier bunch crossing fulfilling the condition:

$$(t_{cl} - R_{cl}/c) \in [-54, -14] \text{ ns} \ , \tag{5.9}$$

which corresponds to about fifteen groups of accidental clusters sources[4]. The times of these clusters were then shifted by a number of bunch crossing periods T_{rf} obtained for each event from the time of the earliest cluster t^f_{cl} as follows:

$$t^n_{cl}(i) \ = \ t_{cl} + \mathrm{T}_{rf} \cdot \mathrm{INT}(\frac{t^f_{cl} - R^f_{cl}/c}{\mathrm{T}_{rf}}) \ , \tag{5.10}$$

and next the acceptance cuts defined in Eq. 5.3 were imposed. This allowed to determine the fraction of events with one or more accidental clusters in the acceptance and, as a consequence, to calculate P_{A1} and P_{A2} (see Tab. 5.1).
The values of P_{A1} and P_{A2} were next used to estimate the probability for a cluster to produce one (P_{S1}) or more fragments (P_{S2}) reconstructed as an additional cluster. In order to do that the true relative photon multiplicities F^{true}_k not affected by the accidental activity or cluster splitting[5] were determined based on the information about the decay chain of the simulated events. Knowing the F^{true}_k values and the determined

[4]The minimum bunch crossing period of DAΦNE is equal to T_{rf} = 2.715 ns.

[5] In the simulations the accidental clusters can be ignored referring to the GEANT KINE indices for particles contributing to each cluster.

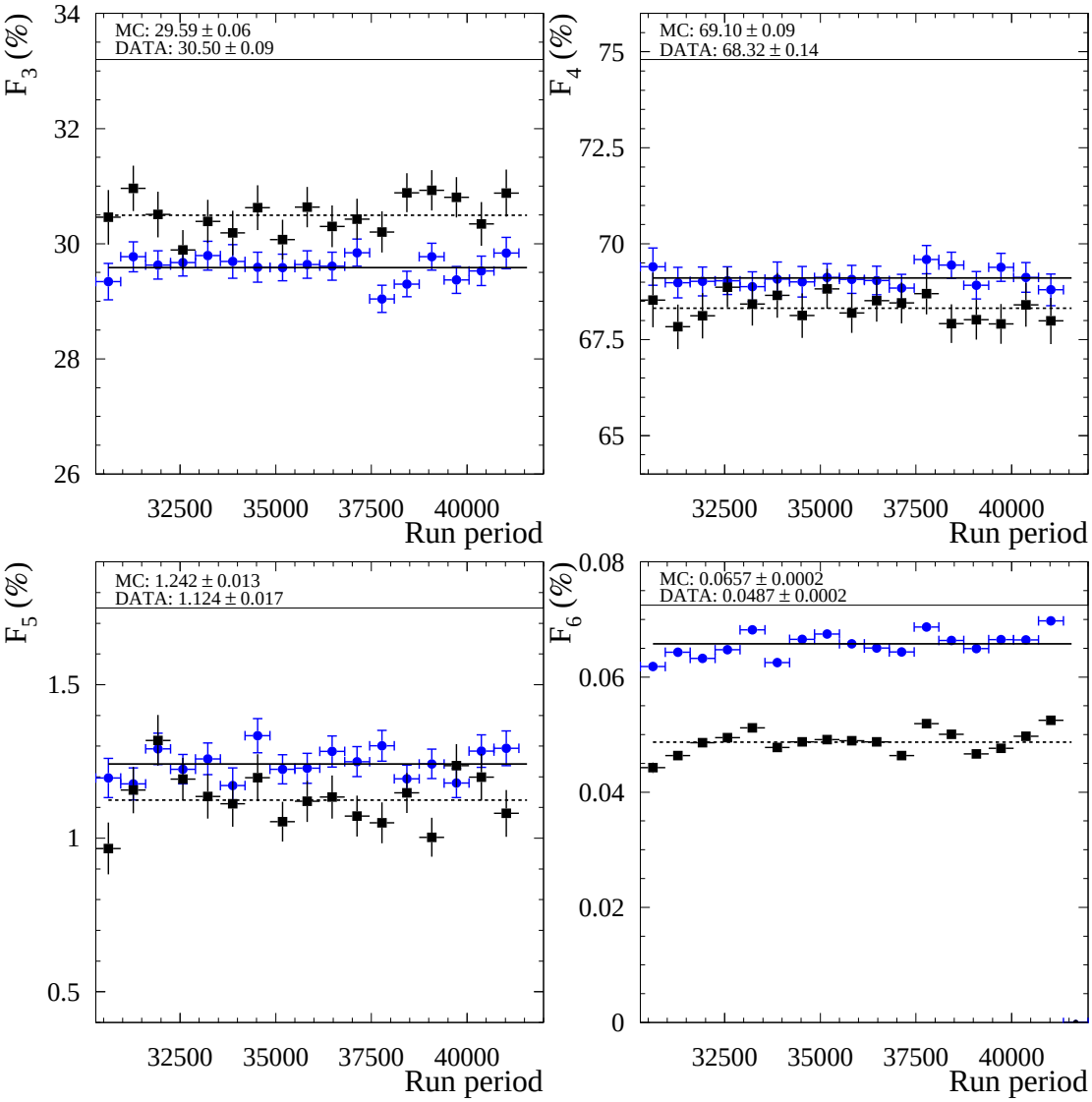


Figure 5.4: Comparison of the F_k distributions for data (black squares) and background simulations (blue circles). The solid and dashed lines denote linear fits ($F_k = const.$) to the spectra of simulations and data, respectively. The results of the fit are reported on the top of each distribution.

	P_{A1} [%]	P_{A2} [%]	P_{S1} [%]	P_{S2} [%]
DATA	0.378 ± 0.004	0.025 ± 0.001	0.30 ± 0.01	0.0103 ± 0.0001
SIMULATIONS	0.492 ± 0.004	0.027 ± 0.001	0.31 ± 0.01	0.0156 ± 0.0002

Table 5.1: The probabilities to find one (P_{A1}) or two (P_{A2}) accidental clusters and to reconstruct one (P_{S1}) or more (P_{S2}) splitted clusters estimated using events in out-of-time window and fit to the F_k distributions, as it is described in the text.

probabilities of accidental coincidence P_{A1} and P_{A2} we can fit the measured F_k distributions treating the P_{S1} and P_{S2} as the free unknown parameters[6]. The obtained splitting probabilities are presented for both data and simulations in Tab. 5.1. These results show that for the simulations there is about 50% more events with two splitted clusters and about 30% more events with one cluster originating from the machine background, which explains the discrepancy for the 6 – gamma events. The technique used to account for this difference is presented in chapter 6.

As described in chapter 4 at the preselection stage we cut on the velocity β_{cr} and energy E_{cr} of the K_L meson, therefore the simulations of its interaction in the calorimeter should be also realistic and precise. The comparison of the β_{cr} and E_{cr} distributions for data and Monte Carlo simulations is presented in Fig. 5.5a and 5.5b. It is clear, that the simulated K_L velocity is in a reasonable agreement with data while there is a big discrepancy in the E_{cr} distribution. Therefore before the cuts optimization another correction for the Monte Carlo simulated events had to be applied. A small correction to the β_{cr} was made adding a shift of 1% multiplied by a Normal – distributed random number. The E_{cr} was instead modified by 2.5% correction increasing every 1 MeV by 0.03%. The resulting distributions are shown in Fig. 5.5c and 5.5d where one can see a much better agreement with data.

Finally applying all the corrections described before we have compared some other simulated inclusive distributions for the 4 – gamma sample with the experimental ones. As it can be seen in Fig. 5.6 the agreement is reasonable so we can proceed with further analysis and counting of the $K_S \to 2\pi^0$ events.

[6]The detailed description of the fit procedure and used probabilistic model is described in Ref. [52], where the technique to measure the P_{A1} and P_{A2} probabilities are also presented more detailed.

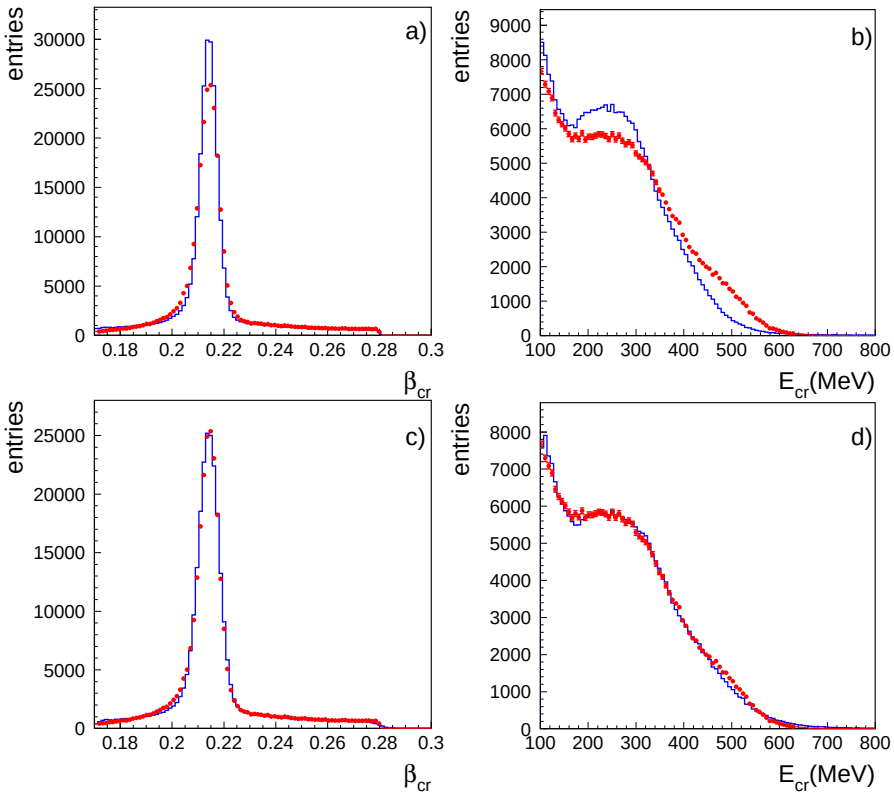


Figure 5.5: Distributions of energy and velocity of the tagging K_L meson for data (red points) and simulations (blue histogram) before (a and b) and after the corrections (c and d). Here only events with four gamma quanta are taken into account.

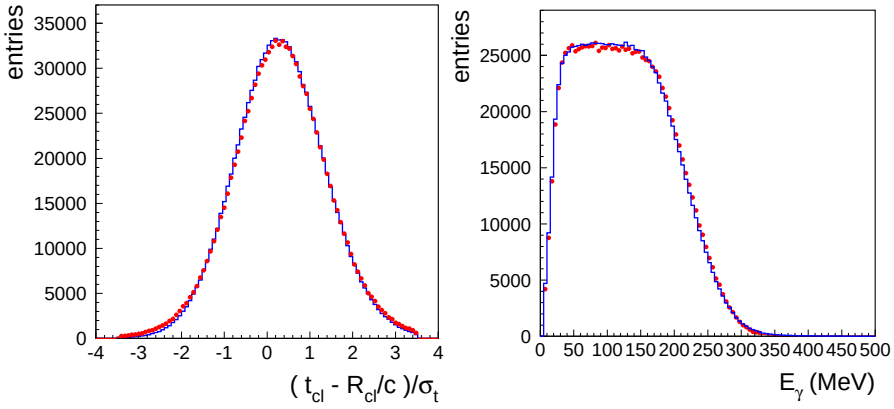


Figure 5.6: Inclusive distributions for the $K_s \to 2\pi^0 \to 4\gamma$ decay after all corrections applied to the Monte Carlo simulations (blue histogram). The red points denote the experimental result.

5.2 Background estimation and counting of the $K_S \to 2\pi^0 \to 4\gamma$ events

Before the final counting of the $K_S \to 2\pi^0$ sample one has to estimate the number of events originating from processes different than $K_S \to 2\pi^0$ for which we have found four reconstructed gamma quanta. To this end we have used the Monte Carlo simulated events of ϕ decays for which the true decay chain is known. Based on this information we have found that the background events constitute a negligible fraction of the 4 – gamma sample amounting to about 0.1%[7]. This allows for counting of the $K_S \to 2\pi^0$ candidates without any further cuts. With the tight requirements for reconstructed K_L energy ($E_{cr} > 150\,\mathrm{MeV}$ and velocity ($0.200 < \beta_{cr} < 0.225$) we have found the following number of events with four reconstructed gamma quanta[8]:

$$N_{2\pi} \;=\; (7.533 \pm 0.018) \times 10^7\;. \tag{5.11}$$

The Monte Carlo simulations allow also for the determination of the $K_S \to 2\pi^0 \to 4\gamma$ selection efficiency. To this end we have used a simulated sample of $N_{tot} \;=\; 59141$ $K_S \to 2\pi^0$ events fulfilling above mentioned tight conditions for β_{cr} and E_{cr}. Next we apply the acceptance cuts and count events with a given number of reconstructed gamma quanta (see Tab. 5.2). The efficiency is then defined as:

$$\epsilon_{2\pi} \;=\; \frac{N^{rec}_{4\gamma}}{N_{tot}}\;. \tag{5.12}$$

$N^{rec}_{4\gamma}$ denotes the number of events with four reconstructed gamma quanta and N_{tot} stands for the total number of simulated $K_S \to 2\pi^0$ events. In both cases we count only events fulfilling the tight K_L tag conditions. Taking into account the estimated

$\boldsymbol{k}$	0	1	2	3	**4**	5	6	7	8
$\boldsymbol{N^{rec}_{k\gamma}}$	25	181	3059	16185	**39012**	636	40	1	2
$\boldsymbol{N^{rec}_{k\gamma}/N_{tot}}[\%]$	0.043	0.31	5.17	27.37	**65.97**	1.08	0.068	0.0017	0.0034

Table 5.2: The number of events $N^{rec}_{k\gamma}$ with a given multiplicity of reconstructed clusters k for N_{tot} = 59141 simulated $\phi \to K_S K_L \to 4\gamma K_L$ events with 0.200 < β_{cr} < 0.225 and E_{cr} > 150 MeV.

selection efficiency: $\epsilon_{2\pi} \;=\; 0.660 \pm 0.002_{stat}$ we can determine the final number of produced events:

$$N_{norm} = \frac{N_{2\pi}}{\epsilon_{2\pi}} = (1.142 \pm 0.005) \cdot 10^8. \tag{5.13}$$

This number will be used for the normalization of the $K_S \to 3\pi^0$ branching ratio.

[7] These are above all the $\phi \to K^+K^-$ events.

[8] The justification of using this set of cuts will be presented in chapter 6.

Chapter 6

Search for the $K_S \to 3\pi^0 \to 6\gamma$ signal

After the K_S tagging via the K_L interactions in the calorimeter the selection of the $K_S \to 3\pi^0$ decay is performed by searching for six photons from the decay of the pions. After the preselection with the conservative[1] K_S tag requirements
($E_{cr} > 100\ \mathrm{MeV}$ and $0.17 < \beta_{cr} < 0.28$) we have found 76689 events with six reconstructed γ quanta. For these events we perform further discriminant analysis to increase the signal to background ratio. As it was in the case of the $K_S \to 2\pi^0$ normalization sample we have considered only calorimeter clusters not associated to any track reconstructed in the drift chamber and imposed acceptance cuts defined with Eqs. 5.3, 5.5 and 5.6.
As it was mentioned in chapter 5, the expected number of background events as well as the analysis efficiency is estimated using the KLOE Monte Carlo simulations. All the processes contributing to the background were simulated with statistics two times larger than the measured data. Moreover, for the acceptance and the analysis efficiency studies the dedicated $K_S \to 3\pi^0$ signal simulations were performed. The signal is generated taking into account the conditions of the KLOE experiment and assuming branching ratio equal to the best known upper limit [16] increased by a factor of 30. Background to the searched $K_S \to 3\pi^0 \to 6\gamma$ signal originates predominantly from the $K_S \to 2\pi^0$ events. The four photons from this decay can be reconstructed as six due to fragmentation of the electromagnetic showers (so called splitting). These events are characterized by two clusters with low energy and position near the place where the true photon hits the calorimeter. The additional fake clusters can be generated also by the accidental coincidence between the ϕ decay event and the DAΦNE background. The other source of background are $\phi \to K_S K_L \to \pi^+\pi^-, 3\pi^0$ events. Methods of suppressing this kind of background will be discussed in the next section.

[1] Such requirements have been used in the previous analysis of the KLOE data [16].

6.1 Discriminating variables and the signal region definition

6.1.1 Rejection of the $K_L \to 3\pi^0$ events

The most dangerous source of background for our analysis are the $\phi \to K_S K_L \to (K_S \to \pi^+\pi^-, K_L \to 3\pi^0)$ events. In this case one of the charged pions can interact in the DAΦNE low – beta insertion quadrupoles producing neutral particles which may ultimately simulate the signal of K_L interaction in the calorimeter, while the K_L meson decays close to the interaction point and produces six photons. To suppress this kind of background we first reject events with charged particles coming from the vicinity of the interaction region. Since K_S decays near the interaction point we reject events with at least one track satisfying:

$$\rho_T = \sqrt{x_{PCA}^2 + y_{PCA}^2} < 4 \text{ cm} \tag{6.1}$$

$$|z_{PCA}| < 10 \text{ cm} , \tag{6.2}$$

where PCA denotes the point of the closest approach of the reconstructed trajectory to the interaction region. In principle one could reject all events with the track reconstructed in the drift chamber. However, this would decrease the reconstruction efficiency of the $K_S \to 3\pi^0$ signal because of the relatively high probability of an accidental coincidence of the real event with tracks generated by DAΦNE background. The choice of conditions defined in Eq. 6.1 minimizes the loss of the signal events due to this effect.

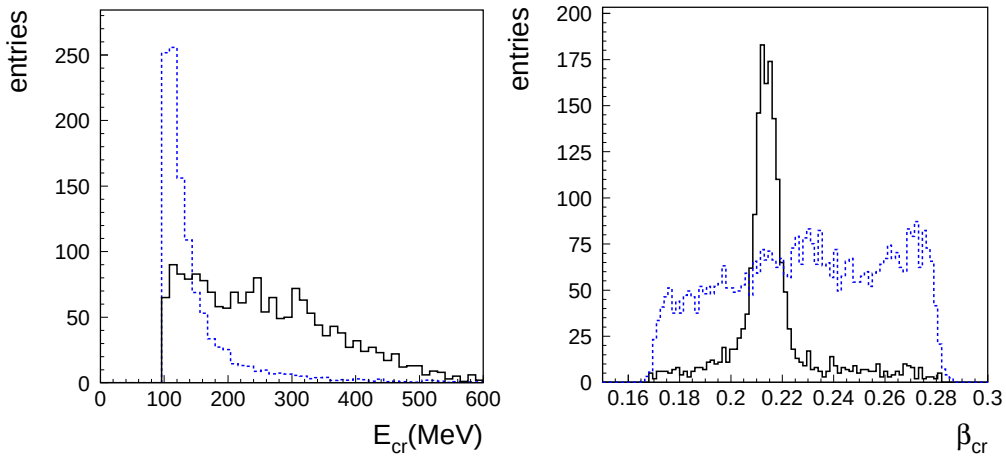


Figure 6.1: Simulated distributions of the reconstructed K_L energy E_{cr} and velocity β_{cr} for the $\phi \to K_S K_L \to (K_S \to 3\pi^0, K_L) \to 6\gamma$ signal (solid) and $\phi \to K_S K_L \to (K_S \to \pi^+\pi^-, K_L \to 3\pi^0) \to \pi^+\pi^- 6\gamma$ background events (dashed) after the conservative cuts on reconstructed β_{cr} and E_{cr} described in Eq. 4.4.

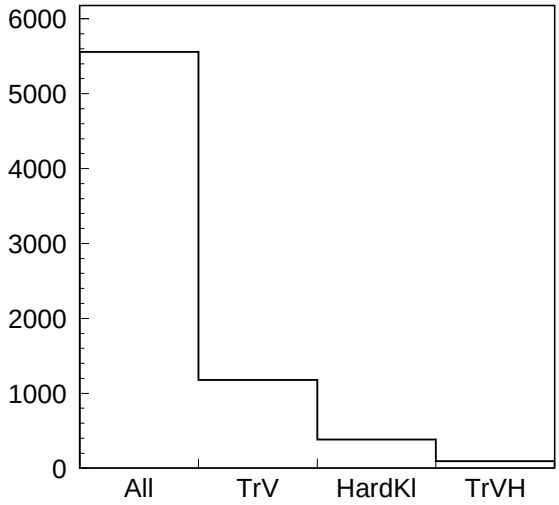


Figure 6.2: The rejection efficiency for the $\phi \to K_S K_L \to \pi^+\pi^-, 3\pi^0$ reaction chain after cutting events with tracks (TrV), after the tight requirements for K_L interaction in the calorimeter (HardKl) and both cuts (TrVH). The result was obtained based on the simulated background sample.

As it is presented in Fig. 6.1 the distribution of the velocity β_{cr} of K_L candidates reconstructed from signals in the calorimeter for events with fake „K_L – crash" is relatively flat, while there is a clear peak around 0.215 for the signal events. Similarly there is a substantial difference in the reconstructed energy spectrum of the interacting K_L mesons and fake „K_L – crash" events. Thus, tightening the cuts on E_{cr} and β_{cr} allows to reject almost all events belonging to this background category:

$$\begin{aligned} E_{cr} &> 150\ \mathrm{MeV} \\ 0.200 < \beta_{cr} &< 0.225\ . \end{aligned} \tag{6.3}$$

These cuts reduce the K_S tagging efficiency from 34% to 23% but we gain a big reduction factor (about 60) on the most important source of background (see Fig. 6.2).

6.1.2 The kinematical fit

In the next stage of the analysis we select only kinematically well defined events. To this end we perform the kinematical fit procedure based on the least squares method with the following set of variables as an input:

- The total energy of the system $\sqrt{s}$
- The momentum P_ϕ and decay vertex of the ϕ meson
- The four – momentum vector and decay vertex of K_S meson

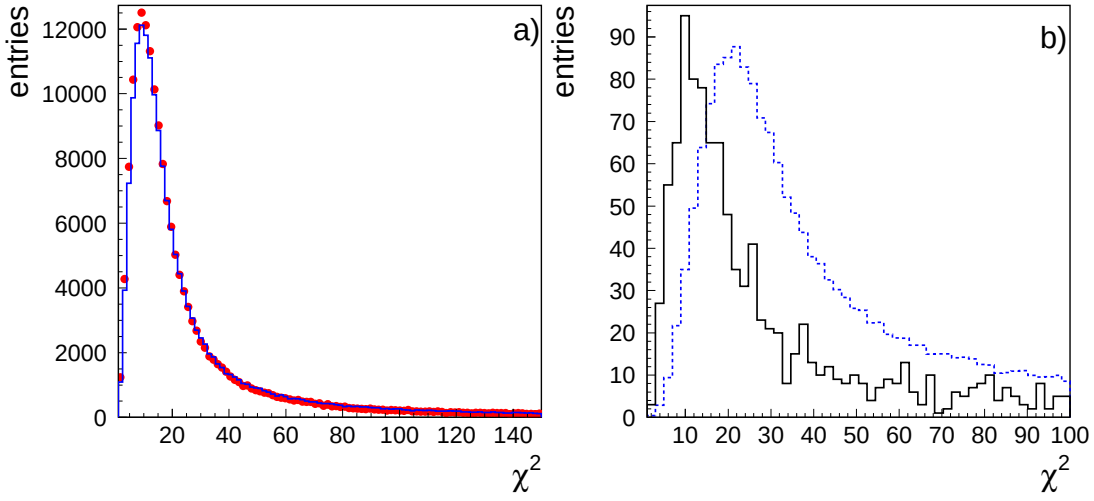


Figure 6.3: a) χ^2 distribution of the kinematical fit for 4γ events of data (red pionts) and simulations (blue histogram); b) The χ^2 distributions from kinematical fit for simulated $K_S \to 3\pi^0$ signal events (solid) and background (dashed).

- Energy of each γ quantum together with its time and position measured in the calorimeter

The initial value of the K_S four – momentum vector is determined for each event using the position of the reconstructed K_L cluster while for $\sqrt{s}$ and P_ϕ we use the mean values measured for each running period using the gathered sample of e^+e^- scattered at large angles. Using this set of variables we can construct the following quadratic form:

$$X^2 \;=\; (\mathbf{Y} - \mathbf{Y_0})^T \mathbf{V}^{-1} (\mathbf{Y} - \mathbf{Y_0}) + \boldsymbol{\lambda} \cdot \mathbf{G}(\mathbf{Y}) \,, \tag{6.4}$$

where $\mathbf{Y_0}$ is a vector of measured variables, $\mathbf{V}$ denotes covariance matrix, $\mathbf{Y}$ denotes the vector of corrected variables fulfilling the kinematical constraints $\mathbf{G}(\mathbf{Y})$ and $\boldsymbol{\lambda}$ is a vector of the Lagrange multipliers. The quadratic form is then minimized with respect to $\mathbf{Y}$ and $\boldsymbol{\lambda}$ leading to the determination of the best corrected variable values. The minimum value of X^2 can be treated as the χ^2 – like variable with a probability function that can be used for hypothesis testing and evaluation of the goodness of the fit. As the constraints we impose the total four – momentum vector conservation, K_S mass requirement and consistency of the time of flight determined from the cluster position of each γ quantum with its time reconstructed in the calorimeter. The developed algorithm was first applied to the kinematically well defined $K_S \to 2\pi^0 \to 4\gamma$ events to test how reliable is the fit procedure. The distributions for data and simulations for this kind of events are shown in Fig. 6.3a. The same distributions for generated background events and $K_S \to 3\pi^0$ signal are shown in Fig. 6.3b. It can be seen that applying a cut on χ^2 around 40 we obtain a small background rejection, about 30%, with a good signal efficiency ($\sim$70$\%$). This does not improve significantly the signal to background

ratio but allows to reject bad quality reconstructed events.

6.1.3 Testing the $3\pi^0$ and $2\pi^0$ hypotheses

In order to reject events with split and accidental clusters we look at the correlation between two χ^2 – like discriminating variables $\chi^2_{2\pi}$ and $\chi^2_{3\pi}$. $\chi^2_{2\pi}$ is calculated by an algorithm selecting four out of six clusters best satisfying the kinematic constraints of the two-body decay, therefore it verifies the $K_S \to 2\pi^0 \to 4\gamma$ hypothesis. The pairing of clusters is based on the difference between reconstructed π^0 masses $M_{\pi^0_1}$ and $M_{\pi^0_2}$ with respect to the PDG value M_{PDG} [19] and on the opening angle of the reconstructed pions trajectories in the K_S center of mass frame $\theta_{\pi\pi}$ which should be equal to 180° for the $K_S \to 2\pi^0$ events. Moreover, we check the consistency of the determination of the K_S four – momentum vector $\mathbb{P}_{K_S}$. It is performed by comparing the $\mathbb{P}_{K_S}$ determined from the reconstructed four – momentum of K_Lwith the sum of the γ quanta four – momenta $\mathbb{P}_{rec} = \sum_{i=1}^{4} \mathbb{P}_{\gamma_i}$. For every possible pairing choice the algorithm calculates the $\chi^2_{2\pi}$ defined as:

$$\chi^2_{2\pi} = \frac{(M_{\pi^0_1} - M_{PDG})^2}{\sigma^2_{2\pi}} + \frac{(M_{\pi^0_2} - M_{PDG})^2}{\sigma^2_{2\pi}} + \frac{(\theta_{\pi\pi} - \pi)^2}{\sigma^2_{\theta_{\pi\pi}}} + \frac{\left(E_{K_S} - \sum_{i=1}^{4} E_{\gamma_i}\right)^2}{\sigma^2_{E_{K_S}}} + \frac{\left(P^x_{K_S} - \sum_{i=1}^{4} P^x_{\gamma_i}\right)^2}{\sigma^2_{P_x}} + \frac{\left(P^y_{K_S} - \sum_{i=1}^{4} P^y_{\gamma_i}\right)^2}{\sigma^2_{P_y}} + \frac{\left(P^z_{K_S} - \sum_{i=1}^{4} P^z_{\gamma_i}\right)^2}{\sigma^2_{P_z}} . \quad (6.5)$$

The minimization of the $\chi^2_{2\pi}$ gives the two photon pairs which out of the six clusters fulfills best the criteria expected for the $K_S \to 2\pi^0 \to 4\gamma$ hypothesis. The resolutions used in Eq. 6.5 were estimated using the $K_S \to 2\pi^0 \to 4\gamma$ normalization sample. The four – momentum vectors of the reconstructed pions were used to make distributions of the differences used for the $\chi^2_{2\pi}$ calculation (see Fig. 6.4), which were then fitted with the Gauss functions allowing for the determination of the variances used in Eq. 6.5. All the values of the parameters are gathered in Tab. 6.1.

The $\chi^2_{3\pi}$ instead verifies the signal hypothesis by looking on the reconstructed masses of three pions. For every choice of cluster pairs we calculate the quadratic sum of the residuals between the nominal π^0 mass and the invariant masses of three photon pairs [21]:

$$\chi^2_{3\pi} = \frac{(M_{\pi^0_1} - M_{PDG})^2}{\sigma^2_{3\pi}} + \frac{(M_{\pi^0_2} - M_{PDG})^2}{\sigma^2_{3\pi}} + \frac{(M_{\pi^0_3} - M_{PDG})^2}{\sigma^2_{3\pi}} . \quad (6.6)$$

As the best combination of cluster pairs we take the configuration with lowest $\chi^2_{3\pi}$. The resolution of pion mass $\sigma_{3\pi}$ was estimated applying the algorithm to the simulated

PARAMETER	DATA	SIMULATIONS
$\sigma_{2\pi 1}$	18.66 ± 0.04	19.24 ± 0.04
$\sigma_{2\pi 2}$	18.84 ± 0.04	19.36 ± 0.04
$\sigma_{E_{K_S}}$	44.07 ± 0.08	46.83 ± 0.09
σ_{P_x}	25.93 ± 0.05	27.55 ± 0.06
σ_{P_y}	26.12 ± 0.05	27.55 ± 0.06
σ_{P_z}	23.48 ± 0.05	24.39 ± 0.06
$\sigma_{\theta_{\pi\pi}}$	0.1238 ± 0.0002	0.1257 ± 0.0002
$\sigma_{3\pi}$	17.0 ± 0.5	17.0 ± 0.5

Table 6.1: List of parameters used in the calculation of $\chi^2_{2\pi}$ and $\chi^2_{3\pi}$. The values were obtained by fitting Gaussian functions to the distributions presented in Fig. 6.4 and to the distributions of pion masses reconstructed by minimization of the $\chi^2_{3\pi}$ value using the simulated signal events.

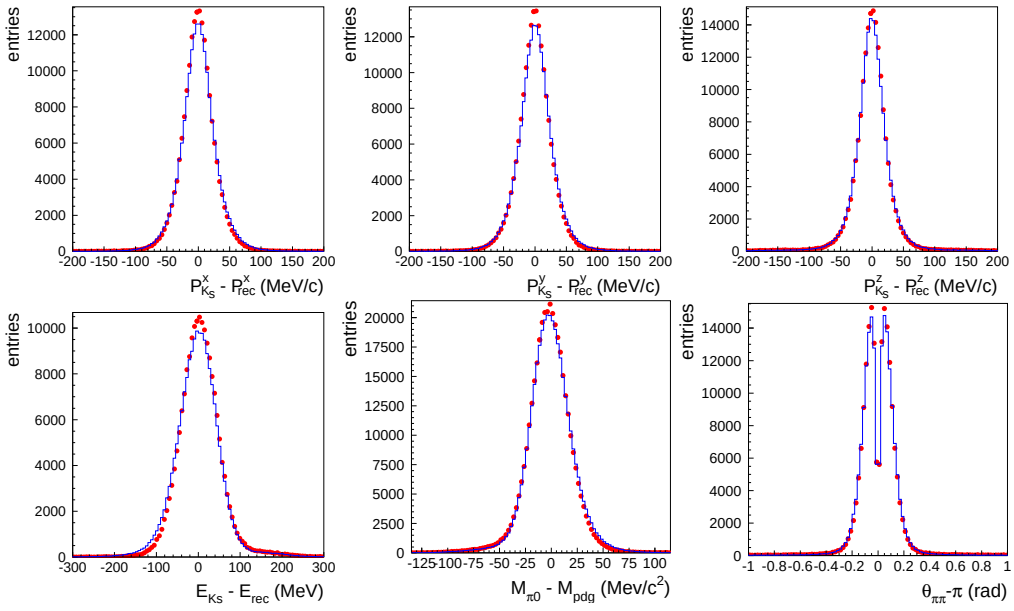


Figure 6.4: Distributions of parameters used in $\chi^2_{2\pi}$ calculation for data (red points) and the simulations of the $K_S \to 2\pi^0$ channel (blue histogram) after the energy scale correction described in Sec. 6.2.

signal events (see Tab. 6.1). In the definition of $\chi^2_{3\pi}$ we do not take into account the difference between $\mathbb{P}_{K_S}$ and $\mathbb{P}_{rec} = \sum_{i=1}^{6} \mathbb{P}_{\gamma_i}$ because in this case it is the same for each combination of photon pairs.

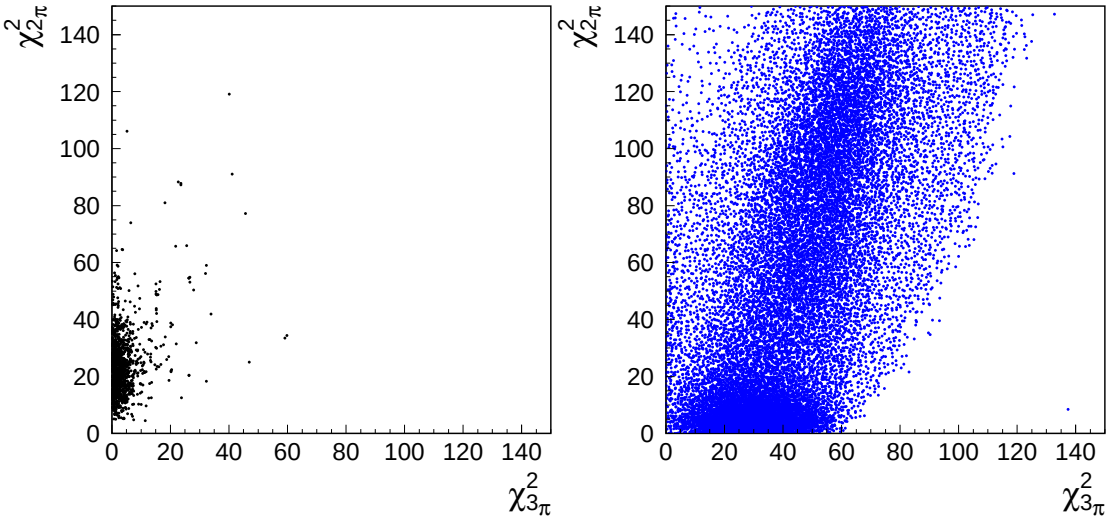


Figure 6.5: Scatter plot of $\chi^2_{2\pi}$ versus $\chi^2_{3\pi}$ for simulated $K_S \to 3\pi^0$ signal (left) and for the background after rejection of the $\phi \to K_S K_L \to \pi^+\pi^-, 3\pi^0$ events (right).

As it is presented in Fig 6.5 the $K_S \to 3\pi^0$ signal is characterized by low values of $\chi^2_{3\pi}$ and relatively high values of $\chi^2_{2\pi}$. Background events are instead spread on the large area of $(\chi^2_{2\pi}, \chi^2_{3\pi})$ plane with a maximum at low $\chi^2_{2\pi}$ being well distinguishable from the signal. Nevertheless in the region populated by signal we find also some background events, mainly the $\phi \to K_S K_L \to \pi^+\pi^-, 3\pi^0$ category even though it is already strongly suppressed by cuts defined with Eqs. 6.1 and 6.3. Further analysis dedicated to the rejection of the background due to the $K_S \to 2\pi^0$ decay is described in the next section.

6.1.4 Improvement of the $K_S \to 2\pi^0$ background suppression

Since we are looking for a very rare decay and have to deal with a large background the rejection power of the data analysis has to be as high as possible. The two additional four – momentum vectors of photon candidates reconstructed based on clusters originating from the machine background or shower fragments results sometimes in an invariant mass close to the mass of π^0. Thus, the $\chi^2_{3\pi}$ algorithm does not distinguish all the $K_S \to 2\pi^0$ decays from the signal and we need another discriminant variable to refine the background rejection.

Events with two accidental clusters can be identified by measurement of the difference ΔE between the K_S energy determined from the reconstructed K_L four – momentum and the sum of energies of four gamma quanta selected by the $\chi^2_{2\pi}$ algorithm. For the

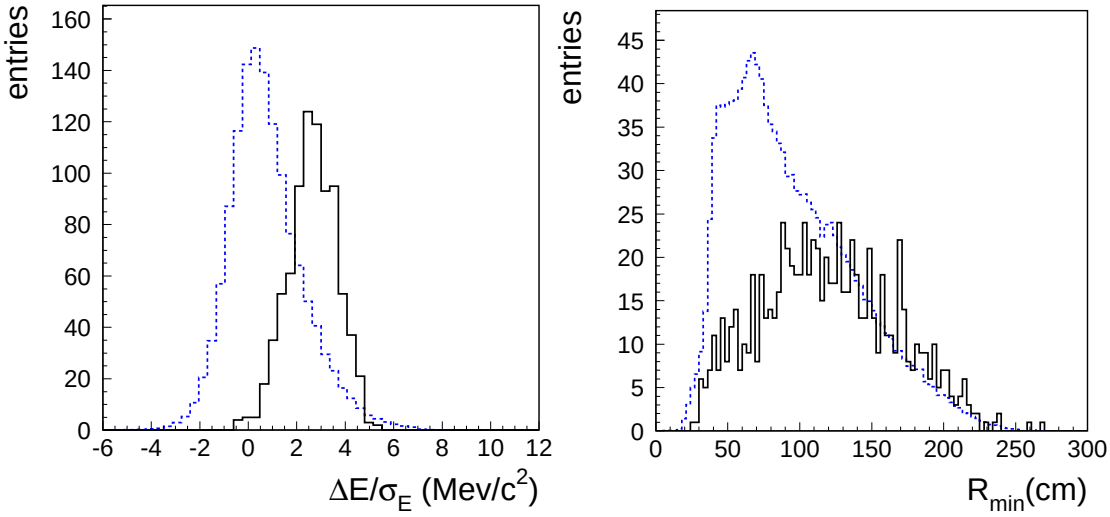


Figure 6.6: Distributions of variables used to refine the rejection of the $K_S \to 2\pi^0$ events. Dashed histogram indicates simulated background events from $K_S \to 2\pi^0$ and solid histogram represents the Monte Carlo simulations of the signal. The distributions are made for events with $\chi^2 < 300$. The variables are described in the text.

$K_S \to 2\pi^0$ background this variable is close to zero since the event is kinematically closed. On the other hand for the $K_S \to 3\pi^0$ events ΔE should peak around 135 MeV since the rejected clusters have an energy comparable to the pion mass. In order to make the cuts as independent as possible of the energy resolution determination we use the normalized ΔE:

$$\Delta E/\sigma_E \;=\; \frac{\left(E_{K_S} - \sum_{i=1}^{4} E_{\gamma_i}\right)}{\sigma_E}\,, \tag{6.7}$$

where the used value of σ_E is equal to the one listed in Tab. 6.1. An example of the $\Delta E/\sigma_E$ distributions for simulated background and signal are presented in the left panel of Fig. 6.6. One can see that cutting around 1.8 allows to reject about 60% of background events keeping the signal efficiency at the level of around 80%.
Further on, events with splitted clusters are suppressed with cut on the distance between center of reconstructed clusters. Here we take advantage of the fact that the distance between splitted clusters is on average smaller than the distance between clusters originating from γ quanta of the $K_S \to 3\pi^0$ decay. For all possible pairs of clusters (i, j) we calculate the distance:

$$R_{ij} \;=\; \sqrt{(x_i - x_j)^2 + (y_i - y_j)^2 + (z_i - z_j)^2}\,, \tag{6.8}$$

where (x_i, y_i, z_i) and (x_j, y_j, z_j) are the position coordinates of clusters reconstructed in the calorimeter. We look then for the minimum of obtained values $R_{min} \;=\; \mathrm{MIN}(R_{ij})$

and impose the following cut:

$$R_{min} > 65 \text{ cm} . \tag{6.9}$$

This suppresses the background by about 30% retaining about 85% of signal events (see right panel of Fig. 6.6). The $\Delta E/\sigma_E$ and R_{min} close the cuts sequence improving the background rejection power of the analysis chain.

6.2 Background estimation

Search for the rare decays like $K_S \to 3\pi^0$ demand a precise knowledge of the background processes. To this end we used realistic Monte Carlo simulations based on GEANT3 package. As it was mentioned in chapter 5 there is a substantial discrepancy between the data and results of the simulation for the six photons sample, which had to be fixed. To this end we first divide the background simulations into categories using for each event information about the decay chain and about particles contributing to each cluster. All the categories are next used in the fitting procedure to the experimental data, which allowed for the determination of the weighting factors for events belonging to each class of simulated background. The procedure used to determine the event weights is described in the following subsection, where we present also small corrections related to the simulated R_{min} distribution and rejection of events with charged particles.

6.2.1 Event weights determination

A below listed classes of background events were recognized[2]:

- Fakes: the $\phi \to K_S K_L \to (K_S \to \pi^+\pi^-, K_L \to 3\pi^0)$ events together with non – $K_S K_L$ channels like $\phi \to K^+K^-$ or $\phi \to \pi^+\pi^-\pi^0$ (about 2%)
- 2A+1A1S: events with two accidental clusters (about 24%) or events with one accidental and one splitted cluster (about 6%)
- 2S: events with two splitted clusters (about 60%) or with more than two accidental or splitted clusters, as well as $K_S \to 2\pi^0$ events with only one splitted or only one accidental cluster (about 8%)

The category called *Fakes* contains, apart from the standard $\phi \to K_S K_L \to (K_S \to \pi^+\pi^-, K_L \to 3\pi^0)$ events, small admixture of the non – $K_S K_L$ background, which is however suppressed by the χ^2 and $\Delta E/\sigma_E$ cuts. As regards other classes of background it is relatively easy to justify the presence of more than two clusters originating

[2] The given fractions of events refer to the simulated sample after the preselection described at the beginning of this chapter.

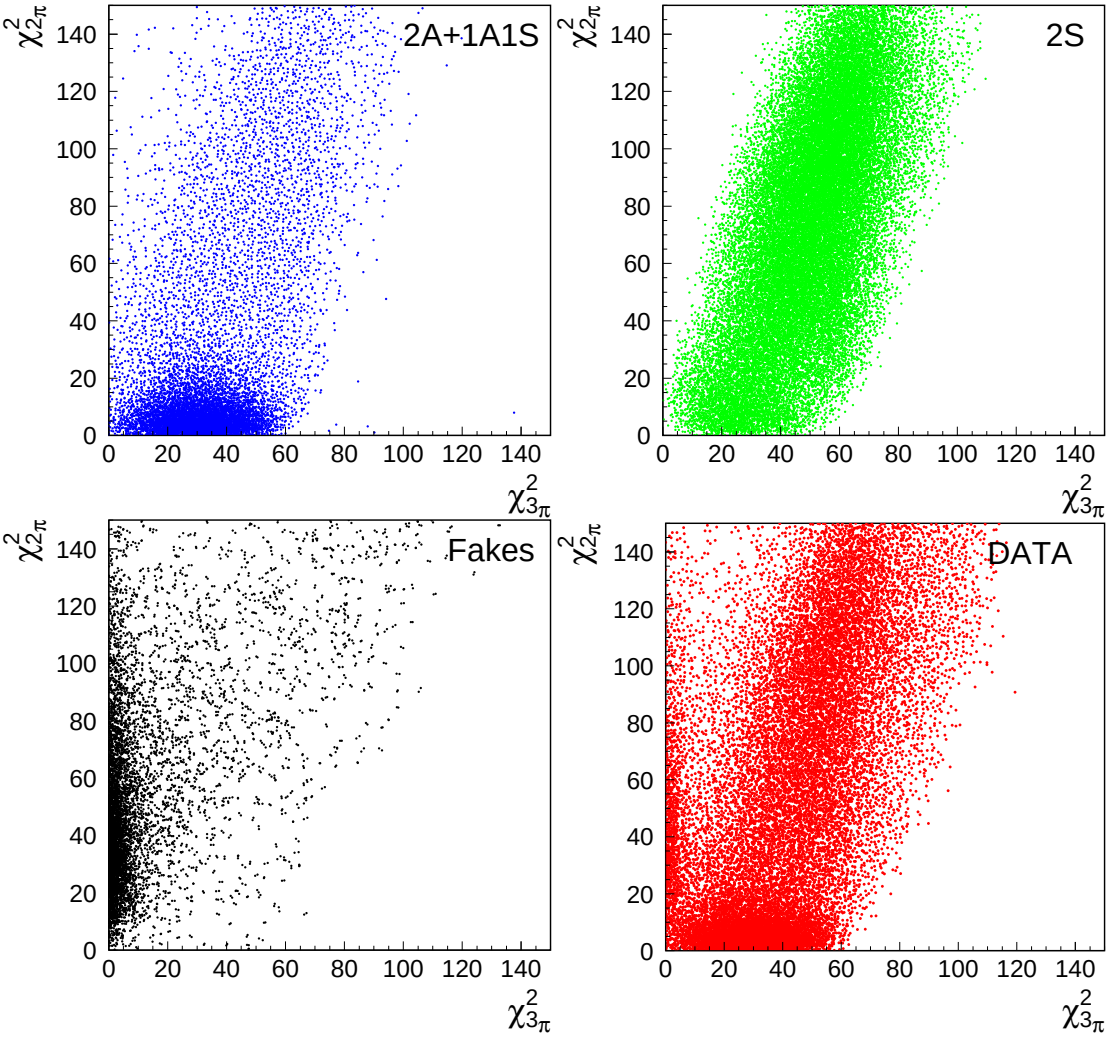


Figure 6.7: The $\chi^2_{2\pi}$ versus $\chi^2_{3\pi}$ scatter plots for different background categories. The label of each plot is defined in the text. The corresponding experimental spectrum is also shown.

from the machine accidental activity or from cluster splitting.

The $K_S \to 2\pi^0$ events with only one splitted or only one accidental cluster in principle should not pass the requirement of the registration of six gamma quanta. However, more detailed analysis revealed, that the additional real cluster can be generated by the initial state radiation or by the wrongly reconstructed K_L cluster[3]. For both data and all the background categories we have made the ($\chi^2_{2\pi}$,$\chi^2_{3\pi}$) scatter plots.

The Monte Carlo distributions were then fitted to the data as a linear combination pro-

[3]It has turned out, that for many events in this category the additional cluster is very close to the place where K_L interacted with calorimeter. Thus they can result from wrongly reconstructed K_L showers.

viding scaling factors W_T for each background category used next to weight events:

$$\mathrm{Data}(\chi^2_{2\pi},\chi^2_{3\pi}) = W_T^{\mathrm{2S}}\cdot \mathrm{Sim}^{\mathrm{2S}}(\chi^2_{2\pi},\chi^2_{3\pi}) + W_T^{\mathrm{2A+1A1S}}\cdot \mathrm{Sim}^{\mathrm{2A+1A1S}}(\chi^2_{2\pi},\chi^2_{3\pi}) + W_T^{\mathrm{Fakes}}\cdot \mathrm{Sim}^{\mathrm{Fakes}}(\chi^2_{2\pi},\chi^2_{3\pi})\ ,$$

where $\mathrm{Data}(\chi^2_{2\pi},\chi^2_{3\pi})$ denotes the experimental $(\chi^2_{2\pi},\chi^2_{3\pi})$ scatter plot and $\mathrm{Sim}(\chi^2_{2\pi},\chi^2_{3\pi})$ stands for the simulated distribution of each background category. The

Category	$\boldsymbol{N_{MC}}$	$\boldsymbol{N_{fit}}$	$\boldsymbol{W_T}$
2A+1A1S	64544 ± 254	26346 ± 236	0.4082 ± 0.0040
2S	145996 ± 382	43446 ± 283	0.2976 ± 0.0021
Fakes	5670 ± 75	6897 ± 148	1.216 ± 0.031

Table 6.2: Scaling factors for Monte Carlo background categories used in the fit to the data. N_{MC} and N_{fit} denote the number of events in each category before and after the fit, respectively.

results of the fit are gathered in Tab. 6.2. The quality of the procedure used to refine the simulations for the six – photon sample can be controlled by the comparison of simulated and experimental inclusive distributions of discriminating variables described in previous sections just after preselection. This comparison is shown in Fig. 6.8 and implies that the agreement between data and background simulations is reasonable after the fit. Another check was done dividing the $(\chi^2_{2\pi},\chi^2_{3\pi})$ plane onto different regions to compare the experimentally observed number of events with expectations based on the Monte Carlo simulations. Five control boxes were chosen around the signal region defined with preliminary cuts on $\chi^2_{2\pi}$ and $\chi^2_{3\pi}$ (see Fig 6.9). The number of events registered in each box is reported in Tab. 6.3, where one can see that simulations results agree with experiment when taking into account the statistical uncertainties calculated using the standard deviations of the scaling factors (see Tab 6.2):

$$\Delta N_{box} = \sqrt{(W_T^{2S}\sqrt{N^{2S}})^2 + (W_T^{2A+1A1S}\sqrt{N^{2A+1A1S}})^2 + (W_T^{Fakes}\sqrt{N^{Fakes}})^2}\ , \tag{6.10}$$

where N denotes the number of events belonging to each background category.
As it can be seen in Fig. 6.10a, despite of application of the weighting factors for different background categories there is still a small discrepancy between data and simulations for the R_{min} discriminant variable. Moreover it turns out, that we reject more events with charged particles having $\beta_{cr} > 0.220$ (see Fig. 6.10c). Therefore, we introduce a small correction shifting the R_{min} by 2 cm smeared with a Normal-distributed random number. The R_{min} distribution after this correction is presented in Fig. 6.10b where we observe much better agreement with data. For the simulated

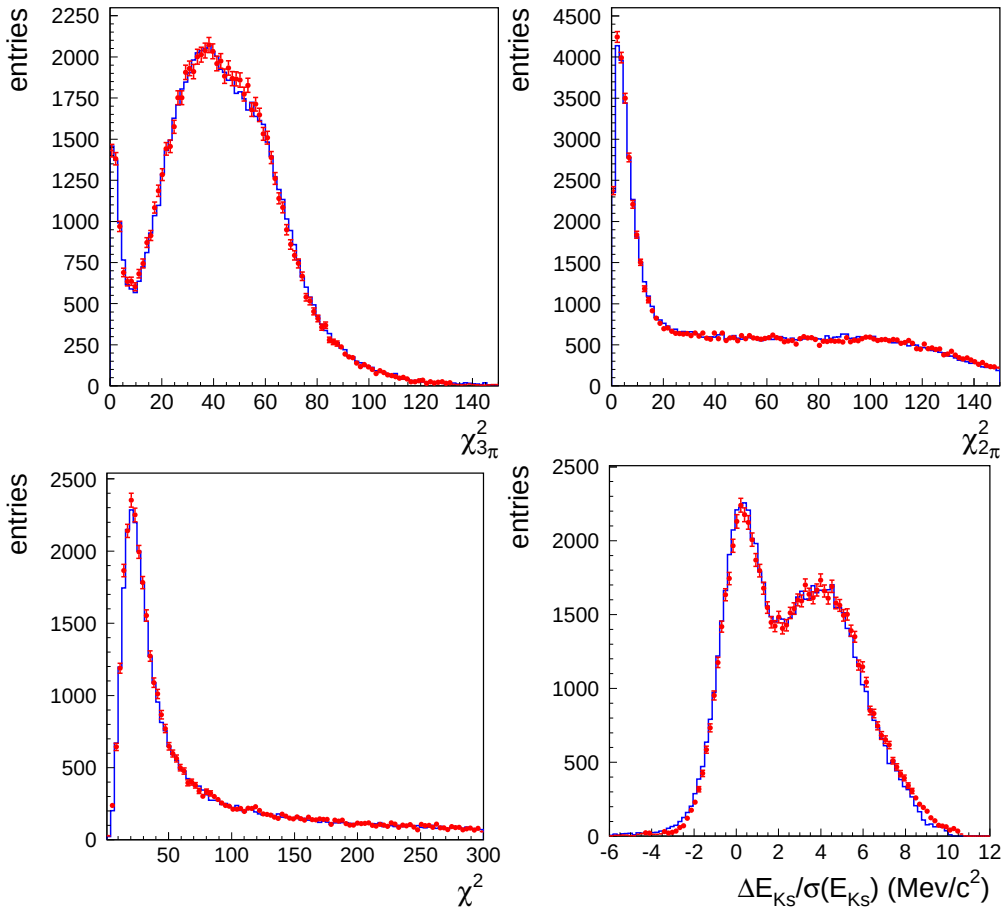


Figure 6.8: Inclusive distributions of discriminating variables for data (red points) and the simulations of the background (blue histograms) weighted with W_T factors as described in the text.

	SBOX	**DOWN**	**UP**	**CDOWN**	**CUP**	**CSBOX**
DATA	200 ± 14	416 ± 21	7 ± 3	14385 ± 120	16321 ± 128	17634 ± 133
MC	228 ± 10	313 ± 12	8 ± 3	14380 ± 134	16143 ± 124	17940 ± 123

Table 6.3: The number of events populating control boxes in the $(\chi^2_{3\pi}, \chi^2_{2\pi})$ plane defined in Fig. 6.9 after tight requirements for the reconstructed K_L energy and velocity.

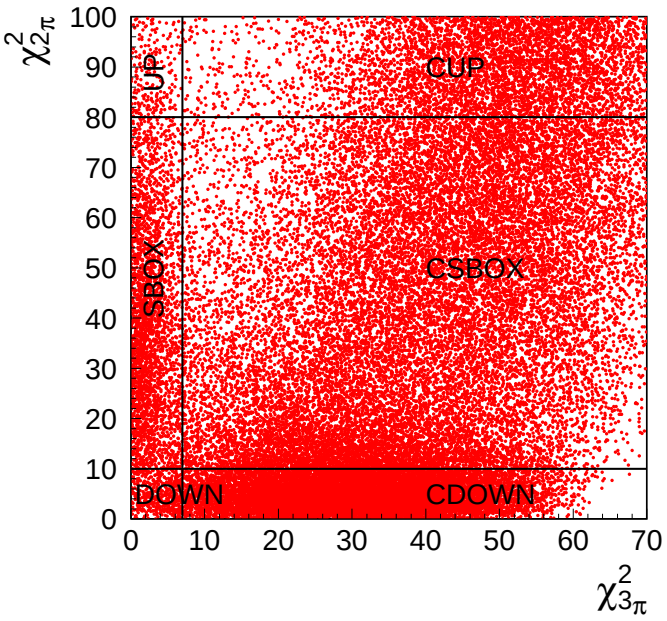


Figure 6.9: Zoom of the $(\chi^2_{3\pi}, \chi^2_{2\pi})$ distribution for data illustrating the division of the plane into control boxes.

events with $\beta_{cr} > 0.220$ belonging to the Fake category a correction based on the „Hit & Miss" method was applied. For each rejected simulated event we draw a random uniformly-distributed number from the range (0.; 1.), if this number was greater than 0.93 the event was passed for the further analysis. The β_{cr} distribution for the rejected events after the correction is presented in Fig. 6.10d.

6.3 Optimization of selection criteria

After all corrections described in last section as well as in chapter 5, after application of the scaling factors the Monte Carlo simulations provide a good description of the measured data. This allows to determine the set of discriminant variables values which provide the best signal to background ratio.
As a next step we optimize the event selection in order to reduce the background as strongly as possible while keeping high signal efficiency. To this end the following cuts were varied:

- the χ^2 of the kinematical fit
- the topological $\Delta E/\sigma_E$ cut
- signal box definition in the $(\chi^2_{3\pi}, \chi^2_{2\pi})$ plane
- R_{min} .

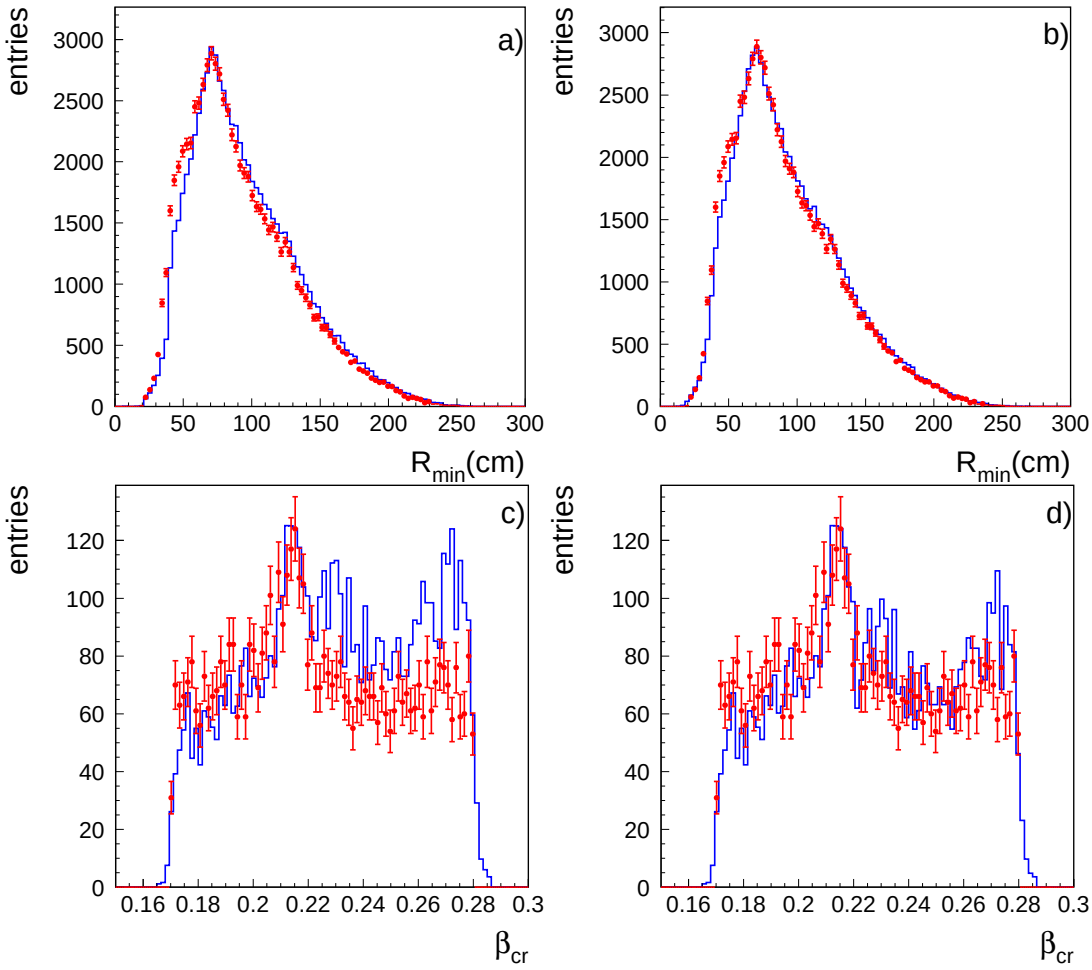


Figure 6.10: The inclusive distributions of R_{min} before (a) and after (b) correction. Plots c and d present β_{cr} spectrum for events with charged particles before and after the correction, respectively. The red points represent the data, while blue histograms denote simulation results.

Each set of the cut values was applied to the simulated background and signal samples excluding events with charged particles coming from the vicinity of the interaction region and for several sets of tight cuts on the reconstructed K_L energy and velocity. This procedure allowed to determine the number of selected background events B and the signal efficiency $\epsilon_{3\pi}$ as a function of the five variables listed above: $B = B(\chi^2, \Delta E/\sigma_E, \chi^2_{3\pi}, \chi^2_{2\pi}, R_{min})$ and $\epsilon_{3\pi} = \epsilon_{3\pi}(\chi^2, \Delta E/\sigma_E, \chi^2_{3\pi}, \chi^2_{2\pi}, R_{min})$. Since the expected number of events at the end of the analysis chain is small we define the following function:

$$f_{cut} \; = \; \frac{N_{up}(B)}{\epsilon_{3\pi}} \; , \tag{6.11}$$

where N_{up} denotes the mean upper limit on the expected number of signal events calculated at 90% confidence level assuming well – known number of background events B[4] [53]. The best choice of cut values is defined as the one which minimizes the f_{cut} value. As the result of the optimization we have obtained the following values of discriminant variables:

$$\begin{aligned} \chi^2 &< 57.2 \\ \Delta E/\sigma_E &\geq 1.88 \\ 4.0 \leq \chi^2_{2\pi} &\leq 84.9 \\ \chi^2_{3\pi} &\leq 5.2 \\ R_{min} &> 65 \; . \end{aligned} \tag{6.12}$$

The signal efficiency corresponding to this set of cuts amounts to:

$$\epsilon_{3\pi} = 0.233 \pm 0.012_{stat}.$$

6.4 Counting of the $K_S \to 3\pi^0$ events

After validation of the Monte Carlo simulations and determination of the optimal set of cut values defined in Eq. 6.12 we preform the discriminant analysis of the experimental six gamma sample preselected using the requirements for the K_L mentioned before:

$$\begin{aligned} E_{cr} &> 150 \text{ MeV} \\ 0.200 < \beta_{cr} &< 0.225 \; , \end{aligned} \tag{6.13}$$

The same analysis was also applied to the simulated background events with six reconstructed gamma quanta fulfilling the tight requirements for K_L listed above. This

[4]The detailed description of the meaning of the mean upper limit and the statistical methods for its estimation will be described in chapter 8.

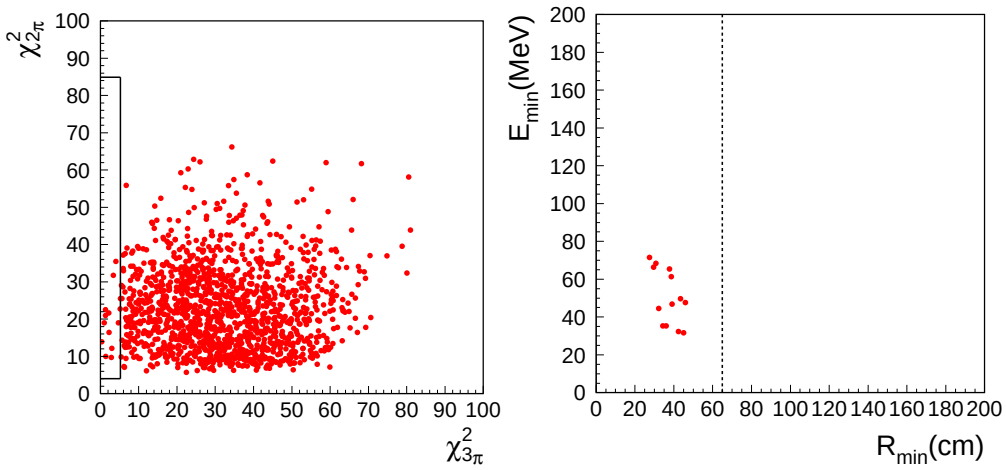


Figure 6.11: Experimental $(\chi^2_{3\pi}, \chi^2_{2\pi})$ distribution after the χ^2 and $\Delta E/\sigma_E$ cuts (left). The right panel presents the scatter plot of R_{min} versus the minimum energy of the cluster E_{min} for events in the Signal Box at the last stage of the analysis. The lines are described in the text.

	all 6 – γ events	**TRV**	$\boldsymbol{\chi^2_{fit}}$	$\boldsymbol{\Delta E/\sigma_E}$	**SBOX**	$\boldsymbol{R_{min}}$
DATA	76689 ± 278	48963 ± 222	16501 ± 129	1400 ± 38	13 ± 4	0 ± 1
MC	76721 ± 446	48984 ± 283	16230 ± 136	1210 ± 21	17 ± 3	0 ± 0.06

Table 6.4: The number of events surviving each subsequent cut. Results for data are given in the first row (DATA) and the second row shows the results for Monte Carlo simulations (MC). TRV denotes the rejection of events with charged particles combined with the tight cuts on the energy and velocity of K_L.

provided the estimation of the expected background at the end of the analysis chain. The experimental scatter plot of ($\chi^2_{3\pi}$ versus $\chi^2_{2\pi}$) after the χ^2 and $\Delta E/\sigma_E$ cuts is presented in the left panel of Fig. 6.11. The solid lines show the signal region defined in Eq. 6.12. As it can be seen in the right panel of Fig. 6.11 all events selected by the Signal Box are characterized by R_{min} less than 65 cm denoted by the dashed line, thus at the end of the analysis chain we have found $N = 0$ of the $K_S \to 3\pi^0$ candidates in data. The expected background contribution amounts to $B_{exp} = 0$.

For the final cross-check of the simulations credibility at each stage of the selection the number of surviving events of both data and Monte Carlo samples were counted. These numbers are reported in Tab 6.4. The statistical uncertainties for the results of simulations were estimated taking into account the scaling factors and using the formula presented in Eq. 6.10. It can be seen that the simulated background is consistent with data after each cut. Moreover, the agreement has been found also both at the beginning and at the end of the analysis in all control boxes in the $(\chi^2_{3\pi}, \chi^2_{2\pi})$ distribution

	SBOX	**DOWN**	**UP**	**CDOWN**	**CUP**	**CSBOX**
DATA	220 ± 15	137 ± 12	5 ± 3	6931 ± 83	15179 ± 123	26491 ± 163
MC	232 ± 11	100 ± 7	4 ± 3	6797 ± 76	14906 ± 116	26962 ± 169

Table 6.5: The population of control boxes in the $(\chi^2_{3\pi}, \chi^2_{2\pi})$ plane right after rejection of events with charged particles imposing the tight cuts on the reconstructed K_L energy and velocity.

	SBOX	**DOWN**	**UP**	**CDOWN**	**CUP**	**CSBOX**
DATA	13 ± 4	0 ± 1	0 ± 1	0 ± 1	0 ± 1	1387 ± 37
MC	17 ± 3	0 ± 0.06	0 ± 0.06	0 ± 0.06	0 ± 0.06	1194 ± 21

Table 6.6: Population of control boxes in the $(\chi^2_{3\pi}, \chi^2_{2\pi})$ plane defined in Subsec. 6.2.1 before the cut on R_{min}.

(see Tab. 6.5 and Tab. 6.6).
Since with the optimal cuts no events were observed only the upper limit on the $K_S \to 3\pi^0$ branching ratio can be determined. The procedure used to estimate the upper limit taking into account the statistical and systematical uncertainties is described in chapter 8.

Chapter 7

Systematic error estimation

In this chapter we present evaluation of the systematic uncertainties for the measurement of the $K_S \to 3\pi^0$ branching ratio. They are related mainly to the determination of the selection efficiencies for the signal and normalization sample $\epsilon_{2\pi}$ and $\epsilon_{3\pi}$, and estimation of the background and cuts used in the discriminant analysis. Moreover we discuss small corrections due to the differences in the efficiencies of the K_S tagging and preselection with so called FILFO filter for the $K_S \to 3\pi^0$ and $K_S \to 2\pi^0$ decays. FILFO (*FILtro FOndo*: background filter) is an off – line procedure identifying background events at a very early stage of the data reconstruction using only information from the calorimeter. Events rejected by FILFO do not enter the track fitting and pattern recognition algorithms which saves CPU-time during events reconstruction or reprocessing [47]. The efficiency of the trigger and cosmic veto for both channels has been neglected due to the fact, that they were found to be very close to 100% in previous KLOE analysis[1] [16]. We conclude giving a summary of the estimated systematic error affecting our result.

7.1 Systematics related to acceptance for the $K_S \to 2\pi^0$ channel

For the normalization sample we have considered the following list of systematic effects related to the determination of the $\epsilon_{2\pi}$ efficiency:

- **Difference in splitting and accidental probabilities between data and simulations**

 As it was mentioned in chapter 5, the probability to find one or more accidental

[1] Since we have used the tighter „K_L – crash" requirements the energy released in the calorimeter by K_L meson was much larger thus the efficiency of trigger is even higher than in the prior analysis.

clusters in the acceptance is slightly different for data and simulations. To estimate the systematic uncertainty originating from this discrepancy we consider the fractions of reconstructed number of photons for the simulated $K_S \to 2\pi^0$ events $F^{true}_{k\gamma} = \frac{N^{rec}_{k\gamma}}{N_{tot}}$ gathered in Tab. 5.2 as the true ones. The presence of additional accidental clusters changes the true fraction $F^{true}_{4\gamma}$ (neglecting the second order effects) to:

$$F'_{4\gamma} \approx F^{true}_{4\gamma} \cdot (1 - P_{A1}) + F^{true}_{3\gamma} \cdot P_{A1}, \tag{7.1}$$

where P_{A1} denotes the probability to find one accidental cluster in the event (see Tab. 5.1). This corresponds to the change $\Delta F_{4\gamma} = (F^{true}_{3\gamma} - F^{true}_{4\gamma}) \cdot P_{A1}$. Therefore the systematic uncertainty originating from the difference of the probabilities ΔP_{A1} for data and Monte Carlo amounts to:

$$\Delta\epsilon_{2\pi}/\epsilon_{2\pi} = \Delta P_{A1} \cdot (F^{true}_{3\gamma} - F^{true}_{4\gamma})/F^{true}_{4\gamma} = 7 \cdot 10^{-4}.$$

Similarly we have calculated the systematic uncertainty due to different probabilities of shower fragmentation for data and simulations. In this case the variation of the true $F^{true}_{4\gamma}$ amounts to:

$$\Delta F_{4\gamma} \approx (3 \cdot F^{true}_{3\gamma} - 4 \cdot F^{true}_{4\gamma}) \cdot P_{S1}\ , \tag{7.2}$$

and the corresponding systematic uncertainty:

$$\Delta\epsilon_{2\pi}/\epsilon_{2\pi} = \Delta P_{S1} \cdot (3 \cdot F^{true}_{3\gamma} - 4 \cdot F^{true}_{4\gamma})/F^{true}_{4\gamma} = 3 \cdot 10^{-4},$$

where ΔP_{S1} is the corresponding difference in the probabilities to generate one splitted cluster for data and Monte Carlo.

- **Correction of the cluster reconstruction efficiency**
 The systematic error due to this correction was estimated conservatively as the difference between the true $f_{4\gamma}$ fractions evaluated with and without correction and amounts to: $\Delta\epsilon_{2\pi}/\epsilon_{2\pi} = 5.2 \cdot 10^{-3}$.

- **Acceptance related effects**
 The number of events counted as a normalization sample was determined in chapter 5 taking into account only events with four reconstructed gamma quanta $N_{norm} = N_{2\pi}/\epsilon_{2\pi}$. Assuming, that events with 3 – 6 reconstructed photons originate from the $K_S \to 2\pi^0$ decay[2] N_{norm} should be consistent with the result determined based on the number of events with 3 – 6 reconstructed photons:

[2] This assumption was checked looking to the true event decay chains for the simulations.

k	0	1	2	3	4	5	6	$\sum_{i=3}^{6}$
N_A^k	141	337	2916	16096	40048	649	39	**56832**
N_R^k	29	43	352	352	148	21	1	**522**
$N_A^k/(N_A^k + N_R^k)[\%]$	83	89	89.2	97.86	99.63	96.9	98	**99.09**

Table 7.1: The number of simulated $K_S \to 2\pi^0$ events accepted (N_A^k) and rejected (N_R^k) by the FILFO filter as a function of the number of reconstructed gamma quanta k. The numbers were obtained without any cuts on the K_L energy and velocity.

Source	$\Delta\epsilon_{2\pi}/\epsilon_{2\pi}[\%]$
Accidental	0.07
Splitting	0.03
Accept. rel.	1.50
Clu. eff. corr	0.52
FILFO	0.46
TOTAL	1.65

Table 7.2: Summary table of the systematic uncertainties on the selection efficiency for the $K_S \to 2\pi^0$ normalization sample.

$N'_{norm} = N_{3-6\gamma}/\epsilon_{3-6\gamma}$[3]. Thus, the difference between these two numbers constitute the measure of the systematic error amounting to $\Delta\epsilon_{2\pi}/\epsilon_{2\pi} = 1.5 \cdot 10^{-2}$.

- **FILFO preselection efficiency**
 To reject the DAΦNE background before the track reconstruction a fast filter FILFO [47] based only on information from calorimeter is applied. Further reconstruction is done only for events which pass this filter. In the Monte Carlo we keep however all the simulated events which allows us to estimate the efficiency. To this end we have considered the sample of $K_S \to 2\pi^0$ events simulated without „K_L – crash" requirements retained and rejected by FILFO (see Tab. 7.1). The efficiency is defined as a ratio of the number of events accepted by the filter with photon multiplicities 3 – 6 to the total number of events with gamma quanta in the same range of multiplicity[4] (see Tab. 7.1), and amounts to: $\epsilon_{2\pi}^F = 0.9909 \pm 0.0004$. This value will be used in the final evaluation of the upper limit presented in chapter 8. As a systematic er-

[3] The $\epsilon_{3-6\gamma}$ was determined using the same simulated $K_S \to 2\pi^0$ sample which was used for the $\epsilon_{2\pi}$ determination (see Tab. 5.2).

[4] We do not consider events with the multiplicities less than 3 because they originate mainly from the wrong T_0 time assignment to the event.

ror contribution related to the preselection with FILFO we take conservatively $\Delta\epsilon_{2\pi}/\epsilon_{2\pi} = (1 - \epsilon^F_{2\pi})/2\epsilon_{2\pi} = 4.6 \cdot 10^{-3}$.

Summary of the different contributions to the systematic uncertainty on $\epsilon_{2\pi}$ is presented in Tab. 7.2, where the total error was evaluated adding all the contributions in quadrature.
Finally, the estimated selection efficiency for the normalization sample amounts to:

$$\epsilon_{2\pi} = (0.660 \pm 0.002_{stat} \pm 0.010_{sys}) \; . \tag{7.3}$$

7.2 Systematics related to the selection efficiency and background for the $K_S \to 3\pi^0$ channel

For the search of the $K_S \to 3\pi^0$ signal the main sources of systematic uncertainties originate from the estimation of background and selection efficiency. As in the case of the $K_S \to 3\pi^0$ channel we have considered also the systematic effects related to the acceptance.
For systematic study of the background we have repeated the analysis changing the parameters values used in $\chi^2_{2\pi}$ and $\chi^2_{3\pi}$ calculation (see Tab. 6.1) as well as varying all the corrections applied to the Monte Carlo simulations, namely:

- using the same resolutions for data and simulations in the $\chi^2_{2\pi}$ definition
- using different resolutions for data and simulations in the $\chi^2_{3\pi}$ definition obtained with control sample consisting of events with charged particles (mainly $K_S \to \pi^+\pi^-; K_L \to 3\pi^0$)
- removing correction on R_{min}
- repeating the analysis with different energy scale corrections
- removing correction on the rejection of events with charged particles
- varying σ_E in the $\Delta E/\sigma_E$ definition ($\sigma_E \pm \delta(\sigma_E)$, where $\delta(\sigma_E)$ denotes the standard deviation of σ_E)
- varying the cuts on the reconstructed K_L energy E_{cr} and velocity β_{cr} arbitrarly by $\pm\, 5\%$.

The full analysis was repeated in total twenty times performing each time one of the systematical checks listed above. For all of the checks we have not observed any changes in the number of background events at the end of the analysis chain.
As in the case of the $K_S \to 2\pi^0$ decay we have considered the following systematic effects for the selection efficiency related to the acceptance cuts:

k	0	1	2	3	4	5	6	7	8
$N^{rec}_{k\gamma}$	2	3	1	12	133	435	597	11	1
$F^{true}_{k\gamma}[\%]$	0.17	0.25	0.08	1.0	11.1	36.4	50.0	0.92	0.09

Table 7.3: The number of events $N^{rec}_{k\gamma}$ reconstructed with a multiplicity of clusters k for N_{tot} = 1195 of $\phi \to K_S K_L \to 6\gamma K_L$ events simulated with 0.200 < β_{cr} < 0.225 and E_{cr} > 150 MeV. $F^{true}_{k\gamma}$ denotes the true fraction defined as $F^{true}_{k\gamma} = N^{rec}_{k\gamma} / \sum_{k=0}^{8} N^{rec}_{k\gamma}$.

- **Splitting and accidental probabilities for data and simulations**
 Based on the same simulated sample of the $K_S \to 3\pi^0$ events which has been used for estimation of the selection efficiency $\epsilon_{3\pi}$ we have determined the true fractions $F^{true}_{k\gamma}$ of the reconstructed number of photons for signal (see Tab. 7.3). The changes of the true $F^{true}_{6\gamma}$ fraction introduced by the presence of accidental clusters amounts to approximately: $\Delta F_{6\gamma} = (F^{true}_{5\gamma} - F^{true}_{6\gamma}) \cdot P_{A1}$. Systematic uncertainty originating form the difference of the probabilities for data and Monte Carlo simulations amounts to:

 $$\Delta\epsilon_{3\pi}/\epsilon_{3\pi} = \Delta P_{A1} \cdot (F^{true}_{5\gamma} - F^{true}_{6\gamma})/F^{true}_{6\gamma} = 7 \cdot 10^{-4}.$$

 Similarly the systematic uncertainty corresponding to the difference in the splitting probabilities has been found to be:

 $$\Delta\epsilon_{3\pi}/\epsilon_{3\pi} = \Delta P_{S1} \cdot (5 \cdot F^{true}_{5\gamma} - 6 \cdot F^{true}_{6\gamma})/F^{true}_{6\gamma} = 3 \cdot 10^{-4}.$$

- **Correction of the cluster reconstruction efficiency**
 The systematic error due to this correction was estimated as in the case of the $K_S \to 2\pi^0$ channel and amounts to $\Delta\epsilon_{3\pi}/\epsilon_{3\pi} = 2 \cdot 10^{-3}$.

- **Energy scale correction**
 As it was described in chapter 5 we have modified the energy scale of the reconstructed gamma quanta in the Monte Carlo simulations to provide a better agreement with data. Systematic error connected with this correction has been estimated by changing the value of the energy shift from 2.2% to 2.6%, and amounts to $\Delta\epsilon_{3\pi}/\epsilon_{3\pi} = 1 \cdot 10^{-2}$.

- **FILFO preselection efficiency for the $K_S \to 3\pi^0$**
 The efficiency of FILFO filter was estimated analogously to the derivation presented in the previous section. The distribution of the $K_S \to 3\pi^0$ events simulated without any requirements for K_L energy and velocity surviving and rejected by FILFO is presented in Tab. 7.4. The estimated efficiency of the fil-

k	0	1	2	3	4	5	6	7	$\sum_{i=3}^{6}$
N_A^k	11	12	1	23	208	658	903	15	1792
N_R^k	0	0	0	0	6	4	1	1	11
$N_A^k/(N_A^k + N_R^k)[\%]$	100	100	100	100	97.2	99.4	99.9	93.8	99.4

Table 7.4: The number of simulated $K_S \to 3\pi^0$ events accepted (N_A^k) and rejected (N_R^k) by the FILFO filter as a function of the number of reconstructed gamma quanta k. The numbers were obtained without any cuts on the K_L energy and velocity.

ter for signal is equal to $\epsilon_{3\pi}^F = 0.994 \pm 0.002$. This value will be used in the final evaluation of the upper limit presented in chapter 8. As a systematic error contribution related to the preselection with FILFO we take conservatively $\Delta\epsilon_{3\pi}/\epsilon_{3\pi} = (1 - \epsilon_{3\pi}^F)/2\epsilon_{3\pi} = 3 \cdot 10^{-3}$.

The last group of systematic uncertainties is connected with the cut sequence used in the discriminant analysis:

- **Energy resolution**
 The systematical uncertainty due to energy resolution was determined by estimation of the selection efficiency $\epsilon_{3\pi}$ with different σ_E values in the $\Delta E/\sigma_E$ definition, which was varied as it was described in the case of systematics related to the background estimation. In this case it amounts to $\Delta\epsilon_{3\pi}/\epsilon_{3\pi} = 1.1 \cdot 10^{-2}$.

- **R_{min} cut**
 The systematic effects related to the R_{min} cut was studied comparing the selection efficiencies evaluated with and without the R_{min} correction. Difference of these two values gives the systematic uncertainty equal to $\Delta\epsilon_{3\pi}/\epsilon_{3\pi} = 9 \cdot 10^{-3}$.

- **χ^2_{fit} cut**
 Systematic effects due to the χ^2_{fit} cut were investigated using the $K_S \to 2\pi^0$ events with four reconstructed gamma quanta. Since the photon multiplicity and energy spectrum of the $K_S \to 2\pi^0$ events differs from the ones for signal we expect differences in the shape of $\chi^2_{fit}/ndof$[5] for the two samples. To estimate the systematic uncertainty related to this difference we have compared the simulated $\chi^2_{fit}/ndof$ distributions for the $K_S \to 2\pi^0$ and $K_S \to 3\pi^0$ events. For both distributions the cumulative curves $f_{2\pi}^{MC}$ and $f_{3\pi}^{MC}$ were determined (see Fig. 7.1a). The ratio $f_{2\pi}^{MC}/f_{3\pi}^{MC}$ which is shown in Fig. 7.1b constitutes the estimation of the contribution to the systematic error. For the cut value used in the

[5] $ndof$ denotes the number of degrees of freedom which amounts to 11 for the $K_S \to 3\pi^0$ events and 9 for the $K_S \to 2\pi^0$ channel.

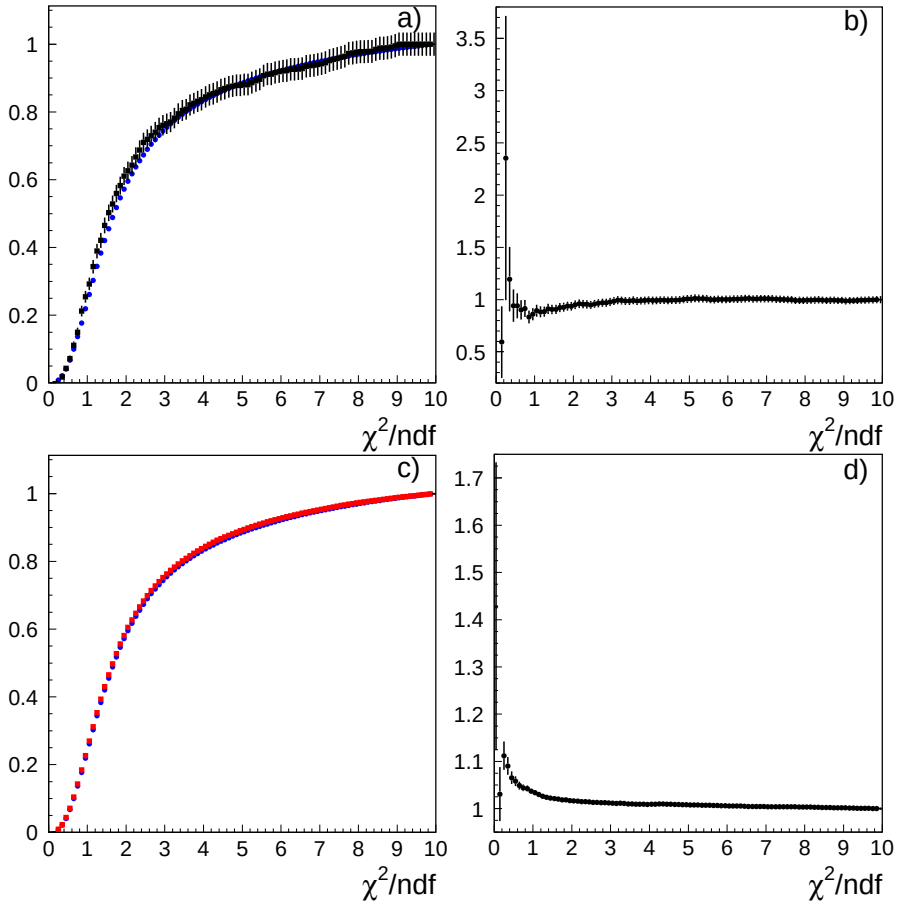


Figure 7.1: a) The cumulative curves of the $\chi^2_{fit}/ndof$ distributions for the simulated $K_S \to 3\pi^0$ (black squares) and $K_S \to 2\pi^0$ (blue circles) samples and b) their ratio; c) Comparison of $\chi^2_{fit}/ndof$ cumulative curves obtained with data (red squares) and simulations (blue circles) for the four gamma events and d) their ratio.

analysis ($\chi^2_{fit}/ndof = 5.2$) it corresponds to $1.22 \cdot 10^{-2}$. Also for the measured $K_S \to 2\pi^0$ events we have constructed a cumulative curve $f_{2\pi}^{Data}$ presented in Fig. 7.1c. The ratio $f_{2\pi}^{Data}/f_{2\pi}^{MC}$ gives us the second part of the systematic error equal to $8 \cdot 10^{-3}$ (see Fig. 7.1 d). Adding the two contributions in quadrature we obtain the total systematic uncertainty on the selection efficiency related to the χ^2_{fit} cut equal to $\Delta\epsilon_{3\pi}/\epsilon_{3\pi} = 1.46 \cdot 10^{-2}$.

Different contributions to the systematic error on $\epsilon_{3\pi}$ are summarized in Tab. 7.5, where the total systematic uncertainty was evaluated adding all of them in quadrature.
The final value of the selection efficiency for the $K_S \to 3\pi^0$ decay amounts to:

$$\epsilon_{3\pi} = 0.233 \pm 0.012_{stat} \pm 0.006_{sys} \; . \tag{7.4}$$

Source	$\Delta\epsilon_{3\pi}/\epsilon_{3\pi}[\%]$
Accidental	0.03
Splitting	0.02
Energy scale	1.00
Clu. eff. corr	0.20
FILFO	0.30
χ^2_{fit}	1.46
Energy resolution	1.10
R_{min}	0.90
TOTAL	2.30

Table 7.5: Summary table of the systematic uncertainties on the selection efficiency for the $K_S \to 3\pi^0$ decay.

7.3 Correction for the different K_S tagging efficiencies for the $K_S \to 3\pi^0$ and $K_S \to 2\pi^0$ decays

The difference in the kinematics and in the photon multiplicity between the $K_S \to 3\pi^0$ and $K_S \to 2\pi^0$ decays creates a small difference in the K_S tagging efficiencies for these channels. This may be result, for example of accidental or splitting clusters which can modify spectrum of the reconstructed K_L energy. To take into account this small effect we have determined the K_S tagging efficiencies independently for each channel using the appropriate simulated sample of events. The estimated efficiencies amounts to

$$\epsilon_{cr}^{2\pi} = (23.65 \pm 0.12) \cdot 10^{-2} \text{ for the } K_S \to 2\pi^0,$$

$$\text{and } \epsilon_{cr}^{3\pi} = (23.90 \pm 0.90) \cdot 10^{-2} \text{ for the } K_S \to 3\pi^0.$$

The ratio $R_{cr} = \epsilon_{cr}^{3\pi}/\epsilon_{cr}^{2\pi} = 1.01 \pm 0.04$ constitutes a correction which will be used in the final evaluation of the upper limit on the $K_S \to 3\pi^0$ branching ratio.

Chapter 8

Upper limit on the $K_S \to 3\pi^0$ branching ratio and $|\eta_{000}|$

8.1 Upper limit on the measured number of $K_S \to 3\pi^0$ decays

The search for the $K_S \to 3\pi^0$ decay presented in this work failed to detect a signal of sufficient statistical significance. Therefore, one can only determine an upper limit on the branching ratio for this decay at a chosen confidence level. A limit on a physical quantity at a given confidence level is usually set by comparing a number of detected events with the expected number of background events in the signal region. The expected background depends strongly on the systematic uncertainties existing in the measurement, therefore they should be taken into consideration in the limit or confidence belt calculation [54].

In the framework of frequentist statistics confidence limits are set using a Neyman construction [55]. This method suffers however from so-called undercoverage when the observable is close to the physics boundary (the actual coverage is less than the requested confidence level). Moreover, constructed confidence intervals may be unphysical or empty, in particular in the case when no events have been observed this method gives no answer for the confidence interval [54].

Feldman and Cousins [56] proposed a new method of confidence interval estimation based on likelihood ratios which automatically provides a central confidence interval or an upper confidence limit decided by the observed data itself (so called unified approach) [54]. However, if the observable is a Poisson distributed variable, there is a background dependence of the upper limit in the case of fewer events observed than expected background. This gives a smaller upper limit for measurements with higher background, which is clearly undesirable. A solution to this problem was proposed by

Roe and Woodroofe taking advantage of a fact that given an observation n, the background b cannot be larger than n [57]. Therefore, the usual Poisson pdf (probability density function) used to construct the confidence interval should be replaced by a conditional pdf. This approach solves the background dependence of the upper limit, however, does not satisfy all the requirements of proper coverage and has problems when applied to the case of a Gaussian distribution with boundaries [54].

All approaches described above do not take into account the systematic uncertainties of estimated background and signal efficiency. Several methods have been developed to incorporate the systematic errors to the calculation of upper limits. An entirely frequentist approach has been proposed for the uncertainty in the background rate prediction [58]. It is based on a two-dimensional confidence belt construction and likelihood ratio hypothesis testing. This method treats the uncertainty in the background as a statistical uncertainty rather than as a systematic one [54].

Several methods combine classical and Bayesian elements (so called semi-Bayesian approaches) for example incorporating systematic uncertainty by performing average over the probability of the detection efficiency [59]. This method is however of limited accuracy in the limit of high relative systematic uncertainties [54]. Conrad *et al.* extended the method of confidence belt construction proposed by Feldman and Cousins. This approach includes systematic uncertainties of both the signal efficiency and background prediction by integration over a pdf parameterizing our knowledge about the sources of the uncertainties [60].

In the framework of Bayes statistics the systematic error is included by modification of the usual conditional pdf with additional probability density functions for the background expectation and signal efficiency [54, 61].

Summarizing, there are many approaches for upper limit estimation and still there is a lot of effort made towards improving these methods and understanding their practical implications. All the approaches mentioned before give in principle different confidence intervals and one has to choose the method depending on the relevance of systematic uncertainties and personal opinion about the Bayesian and classical statistics. The analysis described in this thesis resulted in $n = 0$ observed events with the number of expected background events $b = 0$. In this case all the methods reveal that the upper limit is almost insensitive to the systematic errors of the background estimation and signal efficiency [54, 58, 59, 61]. Moreover, in the case of $n = b = 0$ the upper limit on the number of signal events at the 90% confidence level amounts to 2.21 [58] or 2.33 [54, 59–61] for the systematic uncertainties on background and signal efficiency less than 10%. As it was shown in chapter 7 in our search the systematical errors do not exceed 5%, therefore we assume the upper limit on the number of the $K_S \to 3\pi^0$ events at the 90% confidence level amounting to $N^{up}_{3\pi}(0.9) = 2.33$. This number will be used in the next section for the calculation of the upper limit on $K_S \to 3\pi^0$ branching

ratio.

8.2 Determination of the upper limits on the $K_S \to 3\pi^0$ branching ratio and $|\eta_{000}|$

From the limit on the number of expected signal events one can calculate a limit on the branching ratio. Recalling Eq. 5.2 and taking into account the corrections for the difference in tagging and FILFO preselection efficiencies for signal and the $K_S \to 2\pi^0$ normalization sample described in chapter 7 we obtain the following expression for the branching ratio:

$$BR(K_S \to 3\pi^0) = \frac{1}{R_{cr}} \cdot \frac{\epsilon^F_{2\pi}}{\epsilon^F_{3\pi}} \cdot \frac{N^{up}_{3\pi}(0.9)/\epsilon_{3\pi}}{N_{2\pi}/\epsilon_{2\pi}} \cdot BR(K_S \to 2\pi^0) \,, \qquad (8.1)$$

where R_{cr} denotes the ratio of tagging efficiencies for signal and the $K_S \to 2\pi^0$ normalization sample amounting to $R_{cr} = 1.01 \pm 0.04$. $\epsilon^F_{3\pi} = 0.994 \pm 0.002$ and $\epsilon^F_{2\pi} = 0.9869 \pm 0.0006$ are the FILFO preselection efficiencies determined in chapter 7. The branching ratio for the $K_S \to 2\pi^0$ channel is equal to: $BR(K_S \to 2\pi^0) = 0.3069 \pm 0.0005$ [19]. Taking into account value of the upper limit on the number of expected signal: $N^{up}_{3\pi}(0.9) = 2.33$, the selection efficiency for the $K_S \to 3\pi^0$ channel: $\epsilon_{3\pi} = 0.233 \pm 0.012_{stat} \pm 0.005_{sys}$ and the total number of $K_S \to 2\pi^0$ events: $N_{2\pi}/\epsilon_{2\pi} = (1.142 \pm 0.005) \cdot 10^8$, we have obtained the upper limit on the $K_S \to 3\pi^0$ branching ratio at the 90% confidence level:

$$BR(K_S \to 3\pi^0) \leq 2.7 \cdot 10^{-8} \,.$$

This value is almost five times lower than the latest result $BR(K_S \to 3\pi^0) \leq 1.2 \cdot 10^{-7}$ published by KLOE [16]. The upper limit on the $K_S \to 3\pi^0$ branching ratio can be translated into a limit on the $|\eta_{000}|$ at the 90% confidence level [37]:

$$|\eta_{000}| = \left| \frac{A(K_S \to 3\pi^0)}{A(K_L \to 3\pi^0)} \right| = \sqrt{\frac{\tau_L}{\tau_S} \frac{BR(K_S \to 3\pi^0)}{BR(K_L \to 3\pi^0)}} \leq 0.009 \,,$$

which corresponds to an improvement of the $|\eta_{000}|$ uncertainty by a factor of two with respect to the latest direct search [16].

Chapter 9

Summary and outlook

Kaons have been a remarkably important particles in the development of the Standard Model. The kaon system, being a relatively simple one, played the key role in the discovery of such phenomena as parity and $\mathcal{CP}$ violation, the GIM mechanism and the existence of charm, and was central in the investigation of lepton flavour and $\mathcal{CPT}$ symmetries [62].

$\mathcal{CP}$ violation is deeply related to such fundamental issues as the microscopic time reversibility of physical laws and the origin of the baryonic asymmetry of the universe. It is also the only known phenomenon which allows an absolute distinction between particles and antiparticles [63]. Since the first discovery in the neutral kaon system the $\mathcal{CP}$ symmetry breaking has been a very active field of research. Although at present the main experimental effort is focused on the neutral B and D meson system studies, there are still several interesting open issues in the kaon physics demanding investigation. One of them is the $K_S \to 3\pi^0$ decay which still remains undiscovered. The best published upper limit on its branching ratio $BR(K_S \to 3\pi^0) < 1.2 \cdot 10^{-7}$ is still two orders of magnitude larger than the predictions based on the Standard Model. Therefore, the complete understanding of the $\mathcal{CP}$ violation in the neutral kaon system demands a new high – precision experiments which will contribute also to the $\mathcal{CPT}$ conservation tests.

This work presents the search of the $K_S \to 3\pi^0$ decay based on the data sample gathered in 2004 – 2005 with the KLOE detector operating at the Φ – factory DAΦNE in the Italian National Center for Nuclear Physics in Frascati. DAΦNE is an e^+ and e^- collider optimized to work at the center of mass energy $\sqrt{s} = 1019.45$ MeV. In the two storage rings of DAΦNE 120 bunches of electrons and positrons are stored. Each bunch collides with its counterpart once per turn, minimizing the mutual perturbations of colliding beams. The e^+e^- collisions result in the ϕ meson creation which is almost at rest and decay predominantly to kaon pairs. The decay products are registered using the KLOE detection setup surrounding the e^+e^- interaction point. KLOE consists of large

cylindrical drift chamber surrounded by the electromagnetic calorimeter. The detectors are immersed in the axial magnetic field generated by superconducting solenoid. The K_S mesons were identified via registration of these K_L mesons which crossed the drift chamber without decaying and then interacted with the KLOE electromagnetic calorimeter. The K_S four – momentum vector was then determined using the registered position of the K_L meson and the known momentum of the ϕ meson. The search for the $K_S \to 3\pi^0 \to 6\gamma$ decay was then carried out by the selection of events with six gamma quanta which momenta were reconstructed using time and energy measured by the electromagnetic calorimeter. Background for the searched decay originated mainly from the $K_S \to 2\pi^0$ events with two spurious clusters from fragmentation of the electromagnetic showers or accidental coincidences with signals generated due to particle loss of DAΦNE beams, or from false K_L identification. To increase the signal over background ratio after identification of the K_S meson and requiring six reconstructed photons a discriminant analysis was performed. It started from rejection of events with charged particles coming from the vicinity of the interaction region which suppress the $\phi \to K_S K_L \to (K_S \to \pi^+\pi^-, K_L \to 3\pi^0)$ background events. The further analysis was based on kinematical fit, testing of the signal and background hypotheses and exploiting of the differences in kinematics of the K_S decays into $2\pi^0$ and $3\pi^0$ states.
As a result of the conducted analysis no events corresponding to the $K_S \to 3\pi^0$ decay have been identified. Hence, we have obtained the upper limit on the $K_S \to 3\pi^0$ branching ratio at the 90% confidence level:

$$BR(K_S \to 3\pi^0) \leq 2.7 \cdot 10^{-8} \, . \tag{9.1}$$

This value is almost five times lower than the latest published result. This upper limit can be translated into a limit on the $|\eta_{000}|$ at the 90% confidence level:

$$|\eta_{000}| = \left| \frac{A(K_S \to 3\pi^0)}{A(K_L \to 3\pi^0)} \right| = \sqrt{\frac{\tau_L}{\tau_S} \frac{BR(K_S \to 3\pi^0)}{BR(K_L \to 3\pi^0)}} \leq 0.009 \, , \tag{9.2}$$

which corresponds to an improvement of the $|\eta_{000}|$ uncertainty by a factor of two with respect to the latest direct measurement [16].
However, the upper limit on the $K_S \to 3\pi^0$ branching ratio determined in this work is still about one order of magnitude larger than the prediction based on the Standard Model. Thus, the picture of $\mathcal{CP}$ symmetry violation in the neutral kaon system remains incomplete. Therefore, among several other experiments aiming in the precise measurements of rare and ultra – rare kaon decays [62], we are continuing the research of the $K_S \to 3\pi^0$ decay by means of the KLOE–2 detector. The KLOE–2 collaboration is continuing the physics program of its predecessor. In the last years, a new machine scheme based on the Crab – waist optics and a large Piwinsky angle [64] has been proposed and tested to improve the DAΦNE luminosity. The test has been successful and

presently DAΦNE can reach a peak luminosity of a factor of three larger than previously obtained. The next data taking campaign during 2013 – 2015 will be conducted with a goal to collect total integrated luminosity amounting to about 20 fb^{-1}, which corresponds to one order of magnitude higher statistics with respect to what was used in this search. For the forthcoming run the KLOE performance has been improved by adding new subdetector systems: the tagger system for studies of the meson production in the $\gamma\gamma$ reactions, the Inner Tracker based on the Cylindrical GEM technology and two calorimeters in the final focusing region [65, 66]. These new calorimeters will increase the acceptance of the detector, while the new inner detector for the determination of the K_S vertex will significantly reduce the contribution of the background processes involving charged particles. Increasing the statistics and acceptance of the detector while significantly reducing the background gives the realistic chances to observe the $K_S \to 3\pi^0$ decay for the first time in the near future.

Acknowledgements

I would like to express my highest gratitude to all the people without whom this thesis would not come into being.
First of all, I am deeply indebted to my supervisor, prof. Paweł Moskal, for his invaluable help during my work in his research group. I am very grateful for his patience in correcting all my mistakes and for the time that he spent correcting this thesis (often devoting his free time). I admire his knowledge and attitude towards young people who want to be scientists.
I am very grateful to dr. Stefano Miscetti for being my KLOE supervisor, for his assistance, guidance and patient correction of my mistakes during the data analysis.

I would like to express my appreciation also to:

- dr. Fabio Bossi and dr. Caterina Bloise for making it possible for me to work in the KLOE experiment and to visit Frascati;
- Prof. Bogusław Kamys for all suggestions concerning this work and support during my PhD studies;
- Prof. Lucjan Jarczyk for all his comments and questions during my PhD seminars;
- dr. Matteo Martini and dr. Matteo Palutan for all very useful fortran code and an introduction to the KLOE data analysis;
- all my KLOE – 2 colleagues, especially to: dr. Erika De Lucia, dr. Gianfranco Morello, dr. Antonio De Santis and dr. Salvatore Fiore for all their help and valuable (not only) scientific discussions,for introducing me to the Italian cuisine (especially porchetta in Ariccia);
- dr. Eryk Czerwiński, Jarosław Zdebik and Izabela Pytko for the nice and stimulating atmosphere of work, and all the time we spent together discovering Italy;
- Marcin Zieliński for his help in sending grant applications and all the valuable informations concerning PhD studies;
- all my colleagues from the 03A room: Magdalena Skurzok, Tomasz Bednarski, Tomasz Twaróg, Szymon Niedźwiecki, Wiktor Bardan, Wiktor Parol, Kacper Topolnicki, Krzysztof Kacprzak and Andrzej Pyszniak for a nice atmosphere of work;

Chałbym również serdecznie podziękować swoim Rodzicom za to wszysko czego nauczyłem się od nich i dzięki nim, za ich nieustające wsparcie i miłość. Dziękuję mojej siostrze, która zawsze była przy mnie i pomagała w trudnych chwilach. Jestem również wdzięczny reszcie mojej Rodziny za wsparcie i wszelką pomoc w czasie studiów doktoranckich. Na koniec, chciałbym podziękować Kasi Grzesik, której cierpliwość, nieocenione wsparcie i miłość dodawały mi sił w czasie prowadzenia badań i pisania tej pracy.

Bibliography

[1] A. E. Noether Nachr. d. König. Gessellsch. d. Wiss. zu Göttingen, Math-phys. Klasse., 235 (1918). 1

[2] C. S. Wu, E. Ambler, R. W. Hayward, D. D. Hoppes, and R. P. Hudson, Phys. Rev. **105**, 1413 (1957). 1

[3] R. L. Garwin, L. M. Lederman, and M. Weinrich, Phys. Rev. **105**, 1415 (1957). 1

[4] J. H. Christenson, J. W. Cronin, V. L. Fitch, R. Turlay, Phys. Rev. Lett. **13**, 138 (1964). 1, 8

[5] N. Cabibbo, Phys. Rev. Lett. **10**, 531 (1963). 1

[6] M. Kobayashi, T. Maskawa, Prog. Theor. Phys. **49** (2), 652 (1973). 1

[7] G. Anzivino, J. Phys. Conf. Ser. **335**, 012015 (2011). 1

[8] A. Alavi-Harati *et al.*, Phys. Rev. D **67**, 012005 (2003). 1

[9] A. Passeri, Nucl. Phys. Proc. Suppl. **181-182**, 73 (2008). 1

[10] B. Aubert *et al.*, Nucl. Instrum. Meth. A **479**, 1 (2002). 1, 5

[11] A. Abashian *et al.*, Nucl. Instrum. Meth. A **479**, 117 (2002). 1, 5

[12] A. A. J. Alves *et al.*, JINST **3**, S08005 (2008). 1, 5

[13] F. Wilson, PoS STORI **11**, 027 (2011). 1, 5

[14] M.S. Sozzi, *Discrete symmetries and CP violation*. Oxford University Press, 1st edition (2008); ISBN 978-0-19-929666-8. 1, 2

[15] M. N. Achasov *et al.*, Phys. Lett. B **459**, 674 (1999). 1

[16] F. Ambrosino *et al.*, Phys. Lett. B **619**, 61 (2005). 1, 2, 11, 21, 37, 55, 65, 68

[17] A. Angelopoulos *et al.*, Phys. Lett. B **425**, 391 (1998). 2

[18] A. Lai *et al.*, Phys. Lett. B **610**, 165 (2005). 2

[19] K. Nakamura *et al.* (Particle Data Group), J. Phys. G **37**, 075021 (2010) and 2011 partial update for the 2012 edition. 2, 8, 9, 10, 11, 14, 27, 41, 65

[20] F. Bossi, E. De Lucia, J. Lee-Franzini, S. Miscetti and M. Palutan, Riv. Nuovo Cim. **31**, 531 (2008). 2, 13, 14, 15, 16, 17, 18, 19, 20, 21, 23, 24

[21] M. Silarski, Hyperfine Interact. **211**, 33 (2012). 2, 15, 20, 41

[22] A. D. Sakharov, Pisma Zh. Eksp. Teor. Fiz. **5**, 32 (1967). 5

[23] G. R. Farrar and M. E. Shaposhnikov, Phys. Rev. Lett. **70**, 2833 (1993). 5

[24] G. D. Rochester, C. C. Butler, Nature **160**, 855 (1947). 6

[25] M. Gell-Mann, Phys. Rev. **92**, 833 (1953). 6

[26] T. Nakano and K. Nishijima, Prog. Theor. Phys. **10**, 581 (1953). 6

[27] B. Winstein and L. Wolfenstein, Rev. Mod. Phys. **65**, 1113 (1993). 6

[28] L. Maiani, in Maiani, L. (ed.) *et al.*: *The Second DAΦNE physics handbook*, 3 (1995). 7, 9, 10

[29] E. Aslanides, in Proceedings of *XIV International Conference of Physics in collision*, 365 (1994). 7, 8

[30] Donald H. Perkins, *Introduction to High Energy Physics*, Cambridge University Press, 4th edition (2000); ISBN 0 521 621968. 8, 9

[31] G. Amelino-Camelia *et al.*, Eur. Phys. J. C **68**, 619 (2010). 9

[32] I. Balwierz, PoS STORI **11**, 054 (2011). 9

[33] J. Bernabeu *et al.*, Phys. Rev. Lett. **92**, 131601 (2004). 9

[34] J. Bernabeu *et al.*, Phys. Rev. D **74**, 045014 (2006). 9

[35] A. Di Domenico *et al.*, J. Phys. Conf. Ser. **171**, 012008 (2009). 9, 23

[36] F. Ambrosino *et al.*, Phys. Lett. B **642**, 315 (2006). 9

[37] G. B. Thomson and Y. Zou, Phys. Rev. D **51**, 1412 (1995). 9, 65

[38] E. Abouzaid *et al.*, Phys. Rev. D **83**, 092001 (2011). 9, 10

[39] L. Maiani, N. Paver, in Maiani, L. (ed.) *et al.*: *The Second DAΦNE physics handbook*, 51 (1995). 10, 11

[40] M. Antonelli, G. Barbiellini, S. Bertolucci, C. Bini, C. Bloise, R. Caloi, P. Campana and F. Cervelli *et al.*, Nucl. Instrum. Meth. A **379**, 511 (1996). 13, 19, 20

[41] M. Adinolfi *et al.*, Nucl. Instrum. Meth. A **492**, 134 (2002). 13, 20

[42] G. Finocchiaro *et al.*, Nucl. Instrum. Meth. A **360**, 48 (1995). 13, 15, 17

[43] F. Archilli, Ph.D. Thesis, University of Rome Tor Vergata (2011). 13, 14, 15, 17, 19, 25

[44] F. Ambrosino *et al.*, Nucl. Instrum. Meth. A **534**, 403 (2004). 13, 20, 29

[45] I. Balwierz, Master Thesis, Jagiellonian University (2011). 16

[46] J. Zdebik, Master Thesis, Jagiellonian University (2008). 18, 19

[47] M. Moulson, S. E. Müller, *KLOE Memo* **288** (2004). 21, 55, 57

[48] J. Lee-Franzini and P. Franzini, Acta Phys. Polon. B **38**, 2703 (2007). 23

[49] S. Sinibaldi, T. Spadaro *KLOE Memo* **146** (1998). 24, 25

[50] R. Brun *et al.*, CERN-DD-EE-84-1 (1987). 28

[51] M. Martini, S. Miscetti *KLOE Note* **200** (2005). 29

[52] M. Martini, S. Miscetti *KLOE Note* **201** (2005). 29, 33

[53] J. F. Grivaz and F. Le Diberder, LAL-92-37 (1992). 51

[54] Y. Zhu, Nucl. Instrum. Meth. A **578**, 322 (2007). 63, 64

[55] J. Neyman, Philos. Trans. R. Soc. London Ser. A **236**, 333 (1937). 63

[56] G. J. Feldman and R. D. Cousins, Phys. Rev. D **57**, 3873 (1998). 63

[57] B. P. Roe and M. B. Woodroofe, Phys. Rev. D **60**, 053009 (1999) . 64

[58] W. A. Rolke and A. M. Lopez, Nucl. Instrum. Meth. A **458**, 745 (2001). 64

[59] R. D. Cousins and V. L. Highland, Nucl. Instrum. Meth. A **320**, 331 (1992). 64

[60] J. Conrad, O. Botner, A. Hallgren and C. Perez de los Heros, Phys. Rev. D **67**, 012002 (2003). 64

[61] I. V. Narsky, Nucl. Instrum. Meth. A **450**, 444 (2000). 64

[62] M. S. Sozzi, arXiv:1102.0893 [hep-ex]. 67, 68

[63] M. S. Sozzi and I. Mannelli, Riv. Nuovo Cim. **26N3**, 1 (2003). 67

[64] M. Zobov, D. Alesini, M. E. Biagini, C. Biscari, A. Bocci, M. Boscolo, F. Bossi and B. Buonomo *et al.*, Phys. Rev. Lett. **104**, 174801 (2010). 68

[65] P. Branchini *et al.*, PoS KAON **09**, 012 (2009). 69

[66] P. Branchini *et al.*, PoS KAON **09**, 013 (2009). 69